

Light-dressing of a diatomic superconducting artificial molecule

G. P. Fedorov,^{1,2,3,*} V. B. Yursa,^{4,2} A. E. Efimov,² K. I. Shiiyanov,² A. Yu. Dmitriev,² I. A. Rodionov,^{5,6} A. A. Dobronosova,^{5,6} D. O. Moskalev,⁵ A. A. Pishchimova,^{5,6} E. I. Malevannaya,^{5,6} and O. V. Astafiev^{4,2,7,8}

¹*Russian Quantum Center, Skolkovo village, Russia*

²*Moscow Institute of Physics and Technology, Dolgoprudny, Russia*

³*National University of Science and Technology MISIS, Moscow, Russia*

⁴*Skolkovo Institute of Science and Technology, Moscow, Russian Federation*

⁵*FMN Laboratory, Bauman Moscow State Technical University, Moscow, Russia*

⁶*Dukhov Automatics Research Institute, (VNIIA), Moscow, Russia*

⁷*Physics Department, Royal Holloway, University of London, Egham, Surrey TW20 0EX, United Kingdom*

⁸*National Physical Laboratory, Teddington, TW11 0LW, United Kingdom*

(Dated: June 8, 2020)

In this work, we irradiate a superconducting artificial molecule composed of two coupled tunable transmons with microwave light while monitoring its state via joint dispersive readout. Performing high-power spectroscopy, we observe and identify a variety of single- and multiphoton transitions. We also find that at certain fluxes, the measured spectrum of the system deviates significantly from the solution of the stationary Schrödinger equation with no driving. We reproduce these unusual spectral features by solving numerically the full master equation for a steady-state and attribute them to an Autler-Townes-like effect in which a single tone is simultaneously dressing the system and probing the transitions between new eigenstates. We show that it is possible to find analytically the exact frequencies at which the satellite spectral lines appear by solving self-consistent equations in the rotating frame. Our approach agrees well with both the experiment and the numerical simulation.

I. INTRODUCTION

Over the past twenty years, superconducting artificial atoms (SAAs) were used in numerous experiments in a compelling demonstration of the validity of fundamental quantum mechanical laws [1, 2]. Their Hamiltonians can be pre-designed and engineered which makes them a particularly versatile tool for studies in quantum optics, and high controllability of their parameters allows direct observation of novel physical effects previously inaccessible for natural systems.

One of the most prominent milestones that superconducting quantum circuits have reached so far is the strong coupling with light in circuit QED [3, 4] when the relaxation and decoherence rates appear smaller than the Rabi frequency. Currently, they are surpassing all other implementations of strong coupling in terms of coherence [5]. However, in sharp contrast with natural atoms and molecules, SAAs do not even require confined radiation to implement strong coupling with light: they may be coupled unprecedentedly strongly to free-propagating electromagnetic waves in on-chip waveguides [6] without using cavities at all. In this case, the Rabi frequency may reach 50% of the driven transition frequency [7] which is even beyond strong coupling regime [5]. To correctly describe the atomic behavior in these conditions, the so-called *dressed atom approach* [8] is employed: the radiation has to be directly included in the Hamiltonian of the system and affects its level structure.

Thus far, there have been many experiments with intense driving fields revealing dressing effects in on-chip quantum

optics with artificial atoms [6, 9–16]. In all these works, light dressing of the atom manifests itself through Mollow triplets or Autler-Townes (A-T) splittings of different kinds. However, despite the recent successes in control of large arrays of interacting SAAs [17–19], there were no experiments concerning the behavior of similar composite structures under a strong drive. While there were studies on dressing of multi-atomic systems in a cavity [20–23], dressing by an external free field is no less attractive since its frequency may be easily tuned into resonance with any transition of the system. Moreover, the drive amplitude is also easier to tune than the coupling strength for cavity-dressed systems.

In this work, we study a pair of strongly coupled artificial atoms: a superconducting artificial molecule [24] (SAM). We use two Xmon-type transmons [25, 26] interacting with each other both through a cavity bus [27] and a direct capacitance. Microwave radiation is applied to this system through an on-chip coplanar waveguide antenna while its state can be monitored by joint dispersive readout using the same cavity [28]. Examining our high-resolution spectroscopic data, we find that strong interaction with microwaves not only results in a rich variety of multiphoton transitions of various orders between SAM states, but also significantly modifies its level structure. Even in a simple diatomic molecule, this leads to complex Autler-Townes-like effects involving single- and multiphoton transitions that can only be explained in the dressed picture. Even though the A-T splittings have been investigated before in a wide range of quantum systems (including natural molecules [29, 30]), we find qualitatively new spectral manifestations of light dressing when SAAs are irradiated unequally. We could not find any reports of similar effects in the previous studies of SAAs under a strong driving field. Prior works either involved just a single atom [6, 9–

* gleb.fedorov@phystech.edu

11, 13–16] or demonstrated only the standard spectral signatures known from the quantum optics [12] (see Appendix B). Moreover, previous spectroscopic experiments with coupled transmons were either done at low powers and resolved only the most prominent single-photon transitions [27, 31], or used simultaneous excitation at two distinct frequencies to reach higher energy levels [32], or did not study the spectral data with necessary resolution [33], or used non-tunable transmons [34]. In contrast, we now put a tunable system in a new regime of intense driving which allows us to discover and quantify both experimentally and theoretically its novel unexplored behaviors. Likewise, we could not find reports of such effects in natural molecules, which could in principle be observed there; most probably, this is caused by reduced controllability and coherence compared to superconducting quantum devices.

We believe that our results are valuable to the domain of molecular physics and quantum optics beyond just superconducting Josephson systems since the reported effects are possible to find in any kind of light-matter interaction. In similar conditions, they will emerge for any diatomic molecule regardless of its nature, and modification of the molecular spectra using light is now a topic of active research [35]. In this regard, we note that our theoretical framework can be employed in the analysis of similar effects in the future. Besides, we consider this experiment important for superconducting quantum computing: one should take the observed behaviors into account and control carefully the drive power (for instance, as we will show, the bSWAP gate [34] may be directly affected by light dressing). Finally, the high-power excitation may be applied to directly obtain information about higher energy levels of the system using minimum equipment; this approach can facilitate the scaling of control electronics for superconducting quantum processors (see, i.e. [36]).

The manuscript consists of four main parts and an Appendix. Section I is this introduction; Section II is devoted to the approaches used in our study; Section III contains the results of our experimental and theoretical research, including numerical simulations and analytical analysis; finally, in Section IV we make a conclusion of our work and discuss future prospects. The Appendix contains the details of the theory that we use and additional information about the sample and the measurement techniques.

II. METHODS

A. Device design and control

We have designed the SAM as a pair of tunable Xmon SAAs with asymmetric SQUIDs [37]. They are coupled to a single notch-type $\lambda/4$ resonator [38] ($f_r = 7.34$ GHz, $Q_e \approx 1900$, $Q_i \approx 1100$) which serves for the dispersive readout of their states [28]. In Fig. 1 (a), the optical image of the device is shown, presenting the physical layout of the components. The resonator is connected to a coplanar waveguide through which the readout is performed. At its open end, it is coupled to the transmons by a dual “claw” coupler [26]. Flux lines allowing independent control of the transmon frequencies are

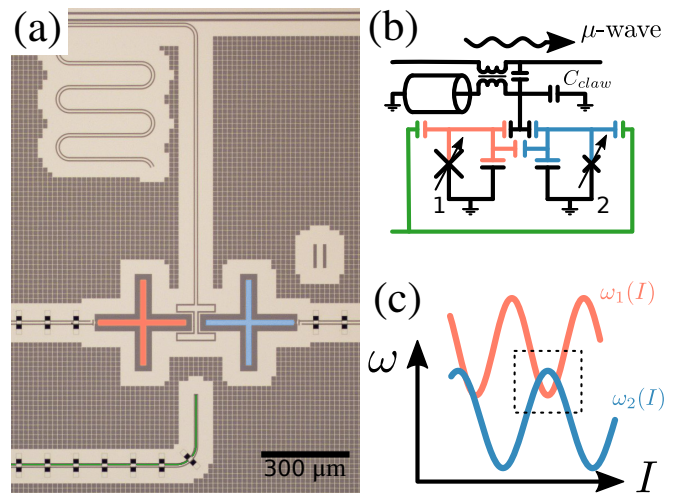


FIG. 1. (a) Optical image of the device (false colored). Two transmons (orange, 1 and blue, 2) are coupled capacitively to a $\lambda/4$ coplanar resonator. Frequency control lines come from both sides, and from below a waveguide for microwave excitation is connected (green). (b) The equivalent electrical circuit. Tunable Josephson junctions are SQUIDs with magnetic flux control. (c) A sketch of the transmon frequencies $\omega_1(I)$ and $\omega_2(I)$ depending on the current I in an external coil when correctly aligned by the individual flux control lines. In this work, we focus on the area inside the dashed rectangle.

coming from the sides, and the excitation waveguide from below directs the microwave signal towards the SAM (green). In Fig. 1 (b), the equivalent electrical circuit of the device is shown. The resonator is inductively and capacitively coupled to the transmission line. Here we simplify the distributed coupling down to lumped elements, as in [39], even though there is a more rigorous approach for this case [40]. The transmons 1 and 2 are false-colored orange and blue, respectively, and their SQUIDs are represented as tunable Josephson junctions. One can note that our design gives rise to two types of coupling in the SAM. The first is the dispersive virtual photon exchange through the multimode cavity [27, 31] and the second is the direct coupling via a mutual capacitance. We find that both of them contribute noticeably to the observed effective coupling strength, but with opposite signs (details can be found in Appendix A). In Fig. 1 (c) we show schematically the transmon frequencies versus the electric current I which we apply to an external coil wound around the sample holder. Since the effective junction of the transmon 1 is larger, its main transition (orange) lies higher in frequency than the one of the second transmon (blue). Using individual flux-control lines, it is possible to align the SAAs so that the lower sweet-spot of the transmon 1 is just below the upper sweet-spot of the transmon 2 (see the dashed rectangle, Fig. 1 (c)). As we will show in the following, this configuration is convenient to track the energies of highly excited levels via multi-photon transitions in a single spectroscopic scan. Additionally, the transmons are better protected from the flux noise near their sweet spots.

B. Quantum-mechanical description

A single transmon SAA can be regarded as an oscillator with a quartic perturbation describing the leading-order anharmonicity [25, 41]. Therefore, in the main text we do not use the charge and the phase operators and write down its Hamiltonian using only the annihilation operator \hat{b} :

$$\hat{H}_{tr}/\hbar = \omega \hat{b}^\dagger \hat{b} + \frac{1}{2} \alpha \hat{b}^\dagger \hat{b} (\hat{b}^\dagger \hat{b} - 1), \quad (1)$$

where ω is the $|0\rangle \rightarrow |1\rangle$, or fundamental, transition frequency and α is the anharmonicity. By applying a magnetic flux to the SQUID (either via an individual on-chip line or via an external coil) it is possible to directly control ω [25]. In our modeling, we take into account the three lowest states of the transmon ($|0\rangle$, $|1\rangle$ and $|2\rangle$).

Eq. 1 describes the SAA without driving. To model a monochromatic microwave signal of frequency ω_d applied through a capacitively coupled transmission line, the following driving term should be included in the Hamiltonian:

$$\hat{H}_d = \hbar \Omega (\hat{b} + \hat{b}^\dagger) \cos \omega_d t, \quad (2)$$

where Ω is the driving amplitude coinciding with the frequency of the Rabi oscillations between $|0\rangle$ and $|1\rangle$.

Next, we assemble the model for two coupled transmons with the corresponding annihilation operators \hat{b} and \hat{c} , the fundamental frequencies $\omega_{1,2}$ and anharmonicities $\alpha_{1,2}$. The corresponding Hamiltonian of the SAM contains two terms representing each transmon, two terms representing the interaction of the transmons with the driving fields at $\omega_d^{(1,2)}$, and the transmon-transmon interaction term:

$$\hat{H} = \hat{H}_{tr}^{(1)} + \hat{H}_{tr}^{(2)} + \hat{H}_d^{(1)} + \hat{H}_d^{(2)} + \hat{H}_{int}, \quad (3)$$

where the superscripts numerate the transmons and $\hat{H}_{int} = \hbar J (\hat{b} + \hat{b}^\dagger)(\hat{c} + \hat{c}^\dagger)$. Strictly speaking, $J = J(\omega_1, \omega_2)$ depends on the transmon frequencies [25], but we take J to be a constant due to its negligible variation for our range of frequencies (see also Appendix A for details).

For brevity, the SAM Hamiltonian without driving terms and the corresponding eigenenergies will be referred below as ‘‘unperturbed’’. Since we use three levels for each transmon, there is a total of nine basis states of the SAM $|i\rangle \otimes |j\rangle = |ij\rangle$, where i and j show the number of excitations in the first and the second transmon, respectively.

In the following, we will also transform Eq. 3 into the frame rotating with both drives by an operator

$$\hat{R} = \exp \left[-it(\omega_d^{(1)} \hat{b}^\dagger \hat{b} + \omega_d^{(2)} \hat{c}^\dagger \hat{c}) \right], \quad (4)$$

arriving at

$$\hat{H}_R = \hat{R}^\dagger \hat{H} \hat{R} - i\hat{R}^\dagger \partial_t \hat{R}. \quad (5)$$

After the transformation and application of the RWA

$$\begin{aligned} \omega_{1,2} &\rightarrow \Delta_{1,2} = \omega_{1,2} - \omega_d^{(1,2)}, \\ \hat{H}_{int} &\rightarrow \hbar J \left[\hat{b}^\dagger \hat{c} e^{it(\omega_d^{(1)} - \omega_d^{(2)})} + \hat{b} \hat{c}^\dagger e^{-it(\omega_d^{(1)} - \omega_d^{(2)})} \right], \\ \hat{H}_d^{(1)} &\rightarrow \frac{\hbar \Omega_1}{2} (\hat{b} + \hat{b}^\dagger), \quad \hat{H}_d^{(2)} \rightarrow \frac{\hbar \Omega_2}{2} (\hat{c} + \hat{c}^\dagger). \end{aligned} \quad (6)$$

Parameter	Transmon 1	Transmon 2
$\omega/2\pi$	5.12 - 6.30 GHz	4.00 - 5.45 GHz
$\alpha/2\pi$	-220 MHz	-220 MHz
T_1	6.82 μ s	4.41 μ s
T_2^*	5.14 μ s	3.33 μ s
$J/2\pi$	8.69 MHz	

TABLE I. SAM model parameters. Transmons are only different in the frequency tuning range and coherence times measured in the lower sweet spot for the 1st one and in the higher sweet spot for the 2nd. The coupling strength J depends on the transmon frequencies and is specified here for $\omega_1/2\pi = \omega_2/2\pi = 5.32$ GHz.

Note that if the transmons are driven at the same frequency, the RWA Hamiltonian is time independent. Below we will use the symbol $\omega_d = \omega_d^{(1)} = \omega_d^{(2)}$ to denote that common frequency of both drives.

Besides the unitary evolution, we also model the incoherent processes of relaxation and dephasing for each transmon using the Lindblad equation with the following collapse operators [42]:

$$\begin{aligned} \hat{\mathcal{O}}_\gamma^{(1)} &= \sqrt{\gamma^{(1)}} \hat{b}, \quad \hat{\mathcal{O}}_\phi^{(1)} = \sqrt{\gamma_\phi^{(1)}} \hat{b}^\dagger \hat{b}, \\ \hat{\mathcal{O}}_\gamma^{(2)} &= \sqrt{\gamma^{(2)}} \hat{c}, \quad \hat{\mathcal{O}}_\phi^{(2)} = \sqrt{\gamma_\phi^{(2)}} \hat{c}^\dagger \hat{c}, \end{aligned} \quad (7)$$

where $\gamma^{(1,2)}$ are the individual relaxation rates, and $\gamma_\phi^{(1,2)}$ are the pure dephasing rates. As one can see, the collapse operators are in a separable form, i.e. acting only upon a single transmon each, which is a valid approach as long as the coupling strength $J \ll \omega_{1,2}$ [43]. Therefore, the complete evolution equation for the system density matrix $\hat{\rho}$ is

$$\partial_t \hat{\rho}_{(R)} = \frac{i}{\hbar} [\hat{\rho}, \hat{H}_{(R)}] + \sum_{\substack{\alpha=\gamma,\phi, \\ i=1,2}} \mathcal{D}[\hat{\mathcal{O}}_\alpha^{(i)}] \hat{\rho}_{(R)} = \mathcal{L} \hat{\rho}_{(R)}, \quad (8)$$

where $\mathcal{D}[\hat{\mathcal{O}}] \hat{\rho} = \hat{\mathcal{O}} \hat{\rho} \hat{\mathcal{O}}^\dagger - \frac{1}{2} \{ \hat{\mathcal{O}}^\dagger \hat{\mathcal{O}}, \hat{\rho} \}$ and \mathcal{L} is the Liouville superoperator, or the Liouvillian; $_{(R)}$ denotes if the Hamiltonian and the corresponding solution density matrix are in the rotating frame with RWA. In this work, we do not alter the dissipator terms when changing the reference frame despite that it may not be correct in general [44].

We summarize the parameters of the SAM model in Table I. The coherence times $T_1 = 1/\gamma$, $T_2^* = 1/(\gamma/2 + \gamma_\phi)$ were measured independently in the lower and the upper sweet spots for transmons 1 and 2, respectively. The remaining parameters were extracted from the fits of the unperturbed model to the observed spectral lines; this procedure will be discussed in more detail in Section III A. The underlying electrical parameters of the transmons are the Josephson energies $E_{J,\Sigma}^{(1)}/h = 24.3$ GHz, $E_{J,\Sigma}^{(2)}/h = 18.3$ GHz, the charging energies $E_C^{(1,2)}/h = 220$ MHz, and the SQUID asymmetries $d^{(1,2)} = 0.7$ (all these parameters are defined as in [25]).

The readout resonator is not included explicitly in the above model since it does not affect the dynamics of the SAM in the

dispersive regime. To model the readout, we use an ad-hoc measurement operator $\hat{M}(f_p)$ that can be obtained by finding the transmission $S_{21}^{(ij)}(f_p)$ (f_p is the probe frequency near the resonator frequency) through the sample after preparing various states $|ij\rangle$ of the SAM. However, in this work we use a simpler method which is to calculate $S_{21}^{(ij)}(f_p)$ via offsetting the experimental resonance curve $S_{21}^{(00)}(f_p)$ measured while the SAM is in the ground state by the corresponding dispersive shifts χ_{ij} [28, 45]. We calculate χ_{ij} with the parameters that can be found in Appendix A according to [25], Eq. D3. Finally, the observable value for any state $\hat{\rho}$ is calculated as $S_{21}^{sim}(f_p) = \text{Tr}[\hat{M}(f_p)\hat{\rho}]$.

C. Numerical solution in *qutip*

Numerical simulations are necessary for studying Eq. 8 since it does not have an analytical solution. We have been using the *qutip* [46] package to simulate the dynamics and to find the steady state of the system for various parameter combinations of the Liouvillian. The source code for the simulations can be found on GitHub [47].

Two distinct modes of simulation were used. The first one is for the Liouvillians that do not explicitly depend on time. In this case, the steady state $\hat{\rho}_{ss}$ of the system should be calculated from the set of linear equations obtained from Eq. 8

$$\partial_t \hat{\rho} = 0 \Rightarrow \mathcal{L} \hat{\rho} = 0 \quad (9)$$

This equation is solved with the *qutip*'s *steadystate* function [48]. This method is applicable when the driving frequency for both transmons is the same.

The second mode is required when it is not possible to avoid the time-dependence of the Liouvillian or if one wants to solve the master equation in the laboratory frame. For example, when the transmons are excited at different frequencies ($\omega_d^{(1)} - \omega_d^{(2)} = \delta \neq 0$), from Eq. 6 we find that even in the doubly-rotating frame, \hat{H}_{int} is oscillating, and it is not possible to simply drop this term in RWA because it is inherent for the SAM. In this case, to find the steady state of the system one can employ the functions *propagator* and *propagator_steadystate* of *qutip*. The propagator is a completely positive map $\Lambda(t_1, t_0) : \hat{\rho}(t_0) \rightarrow \hat{\rho}(t_1)$ describing the time evolution of the system density matrix; for Eq. 8, it is defined as

$$\Lambda(t_1, t_0) = \mathcal{T} \exp \left[\int_{t_0}^{t_1} \mathcal{L}(\tau) d\tau \right], \quad (10)$$

where \mathcal{T} is the time-ordering superoperator. Since the Liouvillian is periodic with a period $T = 2\pi/\delta$, it is possible to calculate the steady state as the eigenvector $\hat{\rho}_{ss}$ of the single-period propagator $\Lambda(T, 0)$ corresponding to its largest eigenvalue [49, 50]. Upon infinitely many applications of Λ

$$\lim_{n \rightarrow \infty} [\Lambda(T, 0)]^n \hat{\rho} = \Lambda(nT, 0) \hat{\rho} \rightarrow \hat{\rho}_{ss}.$$

III. RESULTS

A. Spectroscopy: experiment and numerical simulation

The experiment was conducted as described in Appendix E. We use high-power spectroscopy to probe transitions between the eigenstates of the SAM; the experimental data are shown in Fig. 2 (a). As one can see, besides the fundamental lines that were shown in Fig. 1 (c), some new spectral ones are visible. Their frequency also depends on the applied current, and at several points they become resonant with each other. At three pairs of such resonant points, we observe distinct features shown in insets and marked with Roman numbers I, II, and III. Some secondary details are shown with Arabic-numbered markers. To avoid any possible confusion, we emphasize that by feature I we mean not the usual avoided crossing between $\omega_1(I)$ and $\omega_2(I)$, studied extensively in the past at lower powers. Instead, we call feature I its apparent disappearance and the noticeable change in the shape of the two-photon spectral line that would usually pass straight through it [31].

To check whether the standard theoretical model summarized in Eq. 8 can reproduce the experimental spectrum, we have solved the master equation Eq. 8 finding the steady states of the system $\hat{\rho}_{ss}(I, \omega_d)$ and the corresponding expected measurement outcomes $\text{Tr}[\hat{M}\hat{\rho}_{ss}(I, \omega_d)]$ depending on the external coil current, and the excitation frequency ω_d . The results are shown in Fig. 2 (b) where all the experimental details are immediately reproduced with just nine SAM states. We have solved Eq. 8 in the rotating frame with RWA using Eq. 9 and in the lab frame (using the propagator approach Eq. 10) and did not find any noticeable difference in the results; though, the runtime of a 401×401 point simulation is 9 hours without RWA vs. 3 minutes with RWA. The driving amplitudes $\Omega_{1,2}$ were 20 and 10 MHz, respectively. The parameters of the unperturbed Hamiltonian summarized in Table I were established by fitting the system transition frequencies obtained from numerical diagonalization to the observed spectral lines in Fig. 2 (a). The transmon interaction strength J is usually determined from the size of the avoided crossing between ω_1 and ω_2 . However, in Fig. 2 (a) it is smaller than the linewidths and is not resolved due to the strong drive. By fitting separately measured data at lower power we have obtained $J = 8.69$ MHz. Alternatively, J can be determined from the size of the splitting located at 5.3 GHz and $2.9 \cdot 10^{-4}$ A (or $5.4 \cdot 10^{-4}$ A). It is a well-known effect [32] widely used for implementing cPhase gates on transmons; its size is $(2 \cdot J_{eff})/2$, where $J_{eff} = \sqrt{2}J$ is the corresponding matrix element of \hat{H}_{int} and division by two is required as we observe an intersection between two-photon processes in our data. As can be seen from three slices of Fig. 2 (a), (b) shown in Fig. 2 (c), the numerical results are in a good agreement with the experiment (the spurious resonance is softened).

When modeling the dispersive readout, we noticed that upon SAM excitation the resonance dip was reduced slightly in the experiment. Therefore, the actual observed response was higher than that predicted by only the dispersive shifts. Due to this fact, in Fig. 2 (b), (c) we had to artificially scale the theoretical data up approximately by 30% to obtain the

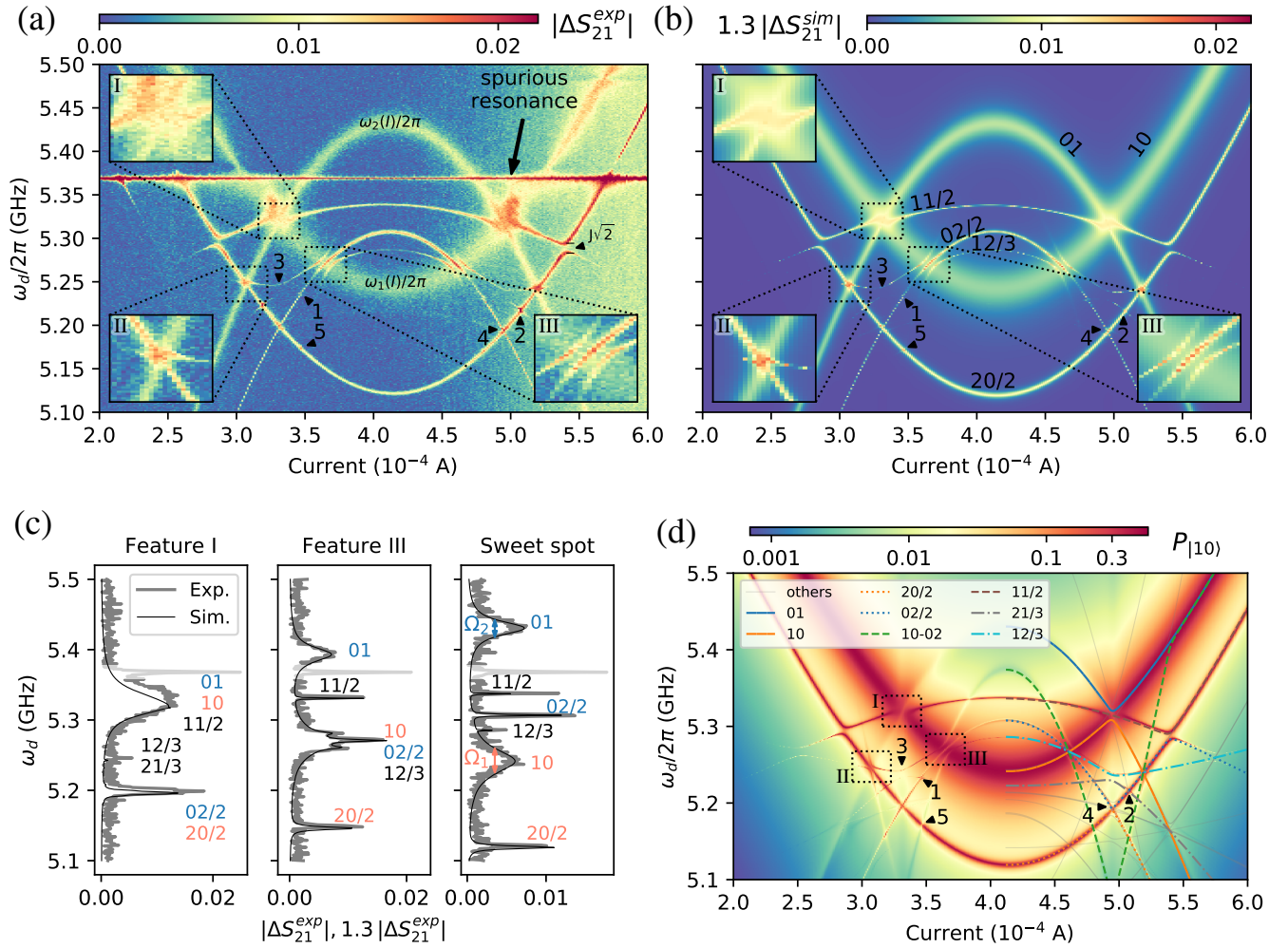


FIG. 2. (a) Measured spectroscopic data. Color shows the absolute deviation $|\Delta S_{21}|(I, \omega_d)$ of the complex transmission through the sample from its value in the lower left corner. Two transmons are aligned as in Fig. 1 (c) and form a symmetric picture. Experimental data contain an additional horizontal line from a parasitic resonance interacting with the readout resonator. Three effects not predicted by the unperturbed model are shown in insets I, II and III; other pronounced features reproduced by the modeling are shown with Arabic markers (see text for description). (b) Numerical simulation reproducing experimental results with labeled transitions (see Section III B for notation). The simulated $|\Delta S_{21}|(I, \omega_d)$ is multiplied by 1.3 to match with the experiment. (c) Slices of (a) and (b) at various currents: 0.333 mA (feature I), 0.365 mA (feature III), 0.411 mA (sweet spot); experiment is gray, simulation is black. Individual Rabi frequencies $\Omega_{1,2}$ may be extracted as FWHM of the spectral lines 10 and 01, respectively. (d) Simulated steady-state population of the state $|10\rangle$ vs. I and ω_d . Lines show various transition frequencies predicted by the unperturbed Hamiltonian. In the legend, the main transitions are labeled near the sweet spot current; if elsewhere any two lines form an avoided crossing, the labels should be swapped after the intersection. Under label “others” we put all the remaining secondary transitions (single- and multiphoton) between each pair levels of the system that fall into the relevant frequency range of the plot.

best match with the experiment. We believe that this problem is connected with the very low observed internal Q-factor of the readout resonator which was 100 times lower than the corresponding Q-factors of the test resonators and the transmons located on the same chip. We have observed this suppression of the readout resonator internal Q-factor for several similar devices, but so far we could not find an explanation for that. However, this problem does not affect our main results which only concern the behavior of the SAM.

Returning to the spectral data, we note that features I, II and III shown in the insets turn out to be impossible to explain using only the unperturbed Hamiltonian; we demonstrate this

by numerical diagonalization of the unperturbed Hamiltonian used in the full simulation. In Fig. 2 (d) we show all possible single and multiphoton transitions between all resulting pairs of the unperturbed eigenlevels that fall into the relevant frequency range. While correctly reproducing, for instance, the avoided crossing labeled as feature 3, the unperturbed model does not produce any transitions following the spectral lines observed in the Roman-numbered areas. For example, one can see that the unperturbed transition 11/2 passes straight in the middle of the avoided crossing between 01 and 10. The experiment and the full simulation demonstrate that the strong drive may change the observed shape of this line.

So far, we have established the fact that the same model SAM yields different spectra depending on the presence of the driving, and that the full model Eq. 8 agrees well with experimental data. To understand the nature of features I, II and III, we describe Fig. 2 in more detail in a separate section below.

B. Analysis of the spectra

a. Identification of the spectral lines. Though it is not possible to describe all of the experimental features with the unperturbed model, we can still use it to identify most of the observed transitions as follows. By numerical diagonalization, we calculate the unperturbed frequencies of the undriven SAM as $\omega_{mn} = (E_n - E_m)/h$ where $n > m$, $n, m = 0..8$. In Fig. 2 (d), we place them over the heatmap data optionally dividing ω_{mn} by some integer n for n -photon processes. Since the number of SAM states is finite, we can quickly find all matches between the heatmap and the calculated eigenlevels.

Next, at the sweet spot, we label the found lines as ij/n . Here, i, j denote the occupation numbers of the transmons 1 and 2, respectively, in the destination state $|ij\rangle$ of the transition; $/n$ is optional for an n -photon process. Such labelling is meaningful because at the sweet spot the transmons are detuned from each other, and thus SAM eigenstates are nearly factorized. Using this notation, we label lines in Fig. 2 (b),(c), as well. The notation is only valid near the sweet spot current before any two lines form an avoided crossing; when they do, their names should be swapped.

As one can see, various multiphoton transitions besides the main lines at $\omega_{1,2}(I)/2\pi$ (or 01 and 10 lines) are visible. The 02/2 and 20/2 are very commonly found for transmons and lie $|\alpha_{1,2}|/2$ lower than the main lines $\omega_{1,2}(I)$. Another two-photon process is the 11/2 line when two SAAs are excited simultaneously. This process is used, for example, for the bSWAP gate [34]; in this work, it is taking part in the formation of feature I. A three-photon process 12/3 is also clearly visible just below the 02/2 line. As we will see, processes 12/3 and 21/3 are involved in forming features III and II, respectively. Notably, transitions 11/2, 21/3, and 12/3 are forbidden when there is no interaction between transmons ($J = 0$). Therefore, it is expected that all Roman-numbered features should only appear with non-vanishing \hat{H}_{int} .

There are also some avoided crossings predicted by the unperturbed model. For a two-transmon SAM they occur at the intersection between lines 01, 10 or 11, 02 (20) visible clearly in Fig. 2 (d). Additionally, marked as feature 3 in Fig. 2, we see an avoided crossing between 12/3, 21/3 at the same current where 01, 10 intersect.

b. Analysing features I, II and III. First, we have reproduced the avoided crossing of feature III in an additional numerical simulation taking only 2 levels for the transmon 1 and three levels for the transmon 2. Upon this, it has become clear that features II and III are actually of the same nature and differ only by the ordering of the transmons: for II, they appear when the transition 01 intersects 20/2, and for III when 10 intersects 02/2; one can see this clearly in Fig. 2 (b).

From Fig. 2 (d) we conclude that avoided crossing in III is between two transitions: 12/3 (three-photon transition $|00\rangle \rightarrow |12\rangle$) and 10–02 (single-photon $|10\rangle \rightarrow |02\rangle$) which are of the same frequency when $\omega_1 = \omega_2 + \alpha_2/2$. The latter process is depopulating 10 and it is better discernible in Fig. 2 (d) than in Fig. 2 (a), (b). For II, the opposite is true: 21/3 and 01–20 are crossing when $\omega_2 = \omega_1 + \alpha_1/2$. From additional measurements and simulations, we find that the splitting depends on the driving power; the experimental and simulated results for feature II are shown in color in Fig. 3 (a), (b), respectively. As one can see, the growth of the splitting with increasing power is linear: it is roughly equal to the FWHM of the 01 spectral line. To fully quantify the shape of this splitting, in Section III C we derive analytical expressions for the dashed curves fitting the spectral lines. In Fig. 3 (c), blue points, we present splitting sizes extracted by fitting that analytical model to the data as in Fig. 3 (a) for various power values of the microwave generator connected to the excitation waveguide. As one can see from the linear approximation of the points, the splitting indeed is simply proportional to the V_{rms} of the signal. From the model, we expect that the minimal distance between the branches of the avoided crossing is equal to $\frac{2\sqrt{3}}{3}\Omega_2$; using this relation, we extract the proportionality coefficient between Ω_2 and V_{rms} of around $2\pi \cdot 0.23$ MHz/mV.

In Fig. 4, we demonstrate a simulated power dependence of feature I: increasing the drive amplitude on one of the transmons while keeping the other one small and constant again result in a certain splitting of the line 11/2. We show only the calculation as long as an experiment is not possible with our sample since we only have a single excitation line and there is no way for us to control the driving amplitudes $\Omega_{1,2}$ independently. We note that two qualitatively different patterns arise depending on which of the transmons is driven stronger than the other. From this and from the shape of the splitting in feature I of Fig. 2 (a), we can infer that $\Omega_1/\Omega_2 \approx 2$ there (also consistent with the 01, 10 linewidths in Fig. 2 (c)). If in contrast both transmons are driven with equal amplitudes, the splitting of 11/2 vanishes. As can be seen from the black dashed lines in Fig. 4, all these cases are explained well by our analytical model described in detail in Sections III C and III D.

From all presented observations, we conclude that effects I – III are caused by light dressing. In case III, the first transmon is dressed by a strong resonant field; in case II, the second one; finally, in case I, both transmons may be dressed at the same time. We will discuss these effects in greater detail in Sections III C and III D.

c. Secondary features. Using Fig. 2 (d), we can get an insight into the features 1 – 5 as well.

Feature 1 is a small avoided crossing between 02/2 and 21/3. It is missing in the unperturbed solution and thus is caused by the light dressing just as I – III. Feature 2 is its twin: 12/3 and 20/2 intersect there but the anticrossing is smaller due to the asymmetry of the driving strengths and is not resolved.

Feature 3 is a large avoided crossing between three-photon processes 12/3 and 21/3. It is predicted by the unperturbed model, and direct diagonalization yields the splitting of $\frac{4}{3}J$. A

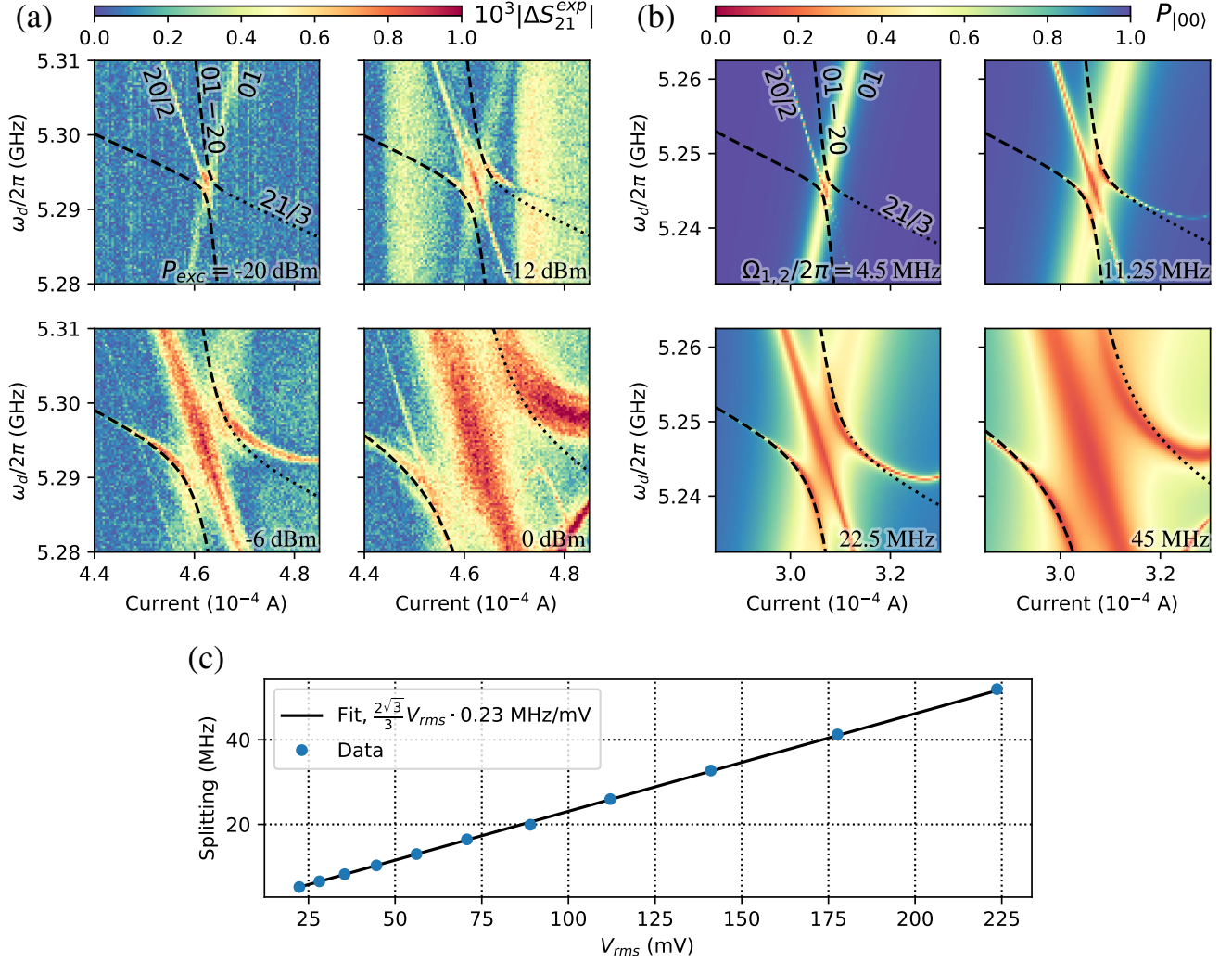


FIG. 3. Power dependence of feature II: experiment, simulation and analytical model. Dashed are the model curves turning to dotted when the model is not expected to be valid (see Sections III C and III D); model values for $\Omega_{1,2}$ are the same for both (a) and (b): $\Omega_{1,2}/2\pi = 4.5, 11.25, 22.5$ and 45 MHz. (a) Experiment (second cooldown; the system parameters are slightly different to those in Fig. 1). The power of the microwave source is increased from -20 to 0 dBm, and the corresponding growth of the splitting and the widths of the spectral lines is observed. (b) Simulation with amplitudes of the driving $\Omega_{1,2}$ equal to the model values; other parameters as in Fig. 2. Note that now colors show the steady-state population of the ground state. (c) Linear dependence of the splitting size on the driving voltage of the microwave source V_{rms} , $\Omega_2/V_{rms} = 2\pi \cdot 0.23$ MHz/mV. From Section III C, the splitting size is $\frac{2\sqrt{3}}{3}\Omega_2$.

remarkable detail here is that the dim lower branch implies the presence of a dark state with respect to the driving operator in the third order.

Feature 4 is also explained by the unperturbed model and is caused by several spectral lines and a pair of avoided crossings near a single point (dotted lines in Fig. 2 (d)). It appears at the point where $02/2$ intersects $20/2$ and is just barely visible in the experimental data because of the noise.

Feature 5 is located at the intersection between $20/2$ and $10-02$, and can be found in the experimental data, too.

In conclusion to this section, we note that when the coupling is turned off ($J = 0$) in the simulation, the system does not demonstrate any of the described details. This means that all these effects can only be attributed to the SAM as a whole.

C. Explaining Roman-numbered effects

Since we had already connected the additional spectral features with light dressing, it is natural to expect an Autler-Townes-like effect to be at the root of the additional spectral lines. For a three-level system, the standard A-T effect is revisited in Appendix B. However, in our case the level structure and the effect itself are more complicated.

First of all, since during the spectroscopy we apply only a single microwave tone ($\omega_d = \omega_d^{(1)} = \omega_d^{(2)}$), it has to be simultaneously the coupler and the probe in the terminology of the standard A-T effect; moreover, the probe must be much weaker than the coupler. It turns out that these condi-

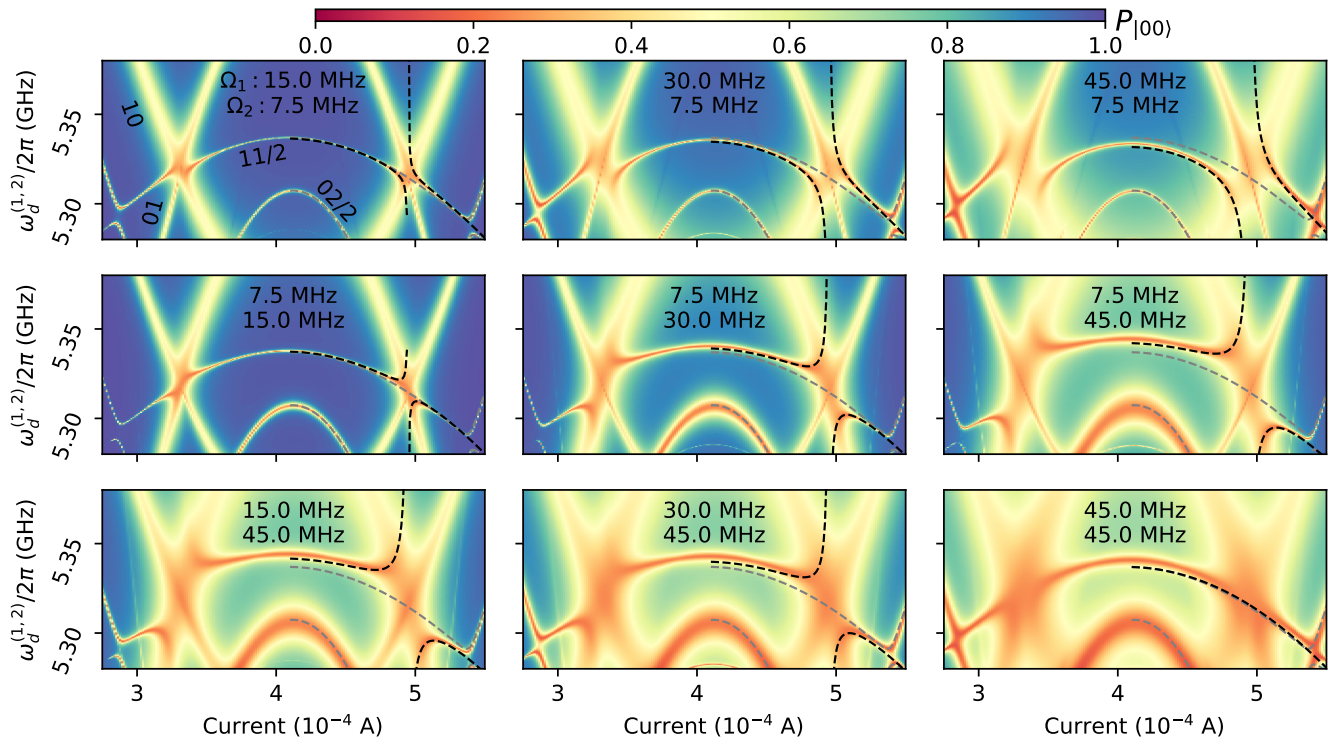


FIG. 4. Simulated power dependence of feature I. With color we show the steady-state population of the ground state when the transmons are driven at the same frequency but at different amplitudes $\Omega_{1,2}$. In the top row (middle row), $\Omega_{1(2)}$ is increased while $\Omega_{2(1)} = \text{const}$, $\Omega_{2(1)} < \Omega_{1(2)}$; two topologically different types of splittings arise depending on which transmon is driven stronger. In the bottom row, we show how the splittings vanish when the weaker drive is increased to match with the stronger one. Gray dashed lines show the unperturbed solution, in black are the model curves based on Sections III C and III D.

tions become satisfied around feature II (III) when $\omega_{2(1)} = \omega_{1(2)} + \alpha_{1(2)}/2$ where we can simultaneously excite transitions 01(10) and 20/2(02/2). Since the two-photon Rabi frequency is much smaller than the single-photon one, it is natural to view the two-photon excitation as the probing process which does not affect the level structure. In contrast, the single-photon excitation is strong enough to dress the system. In other words, for the feature III, the A-T coupling operator is $\hat{H}_d^{(1)}$, and the probing operator is $\hat{H}_d^{(2)}$. However, their separation now is not in frequency, but in the Hilbert subspaces they act upon and in the number of participating photons.

For the feature I, the simultaneously excited transitions are 01, 10 and the two-photon 11/2. In this case, the weak two-photon process is probing transitions in the doubly-dressed SAM. We find that if SAAs are dressed equally, 11/2 does not split, and for it to be distinguishable it is required that $\Omega_{1(2)} \gg \Omega_{2(1)}$.

Below, we give a detailed explanation of features II and III, and finally, I.

a. Features II and III. In Fig. 5, we fully identify the transitions between dressed states that are involved in the A-T-like effect for feature III. For simplicity, we will temporarily assume that the transmons are driven at different frequencies $\omega_d^{(1)}$ and $\omega_d^{(2)}$ (this assumption will be lifted in the following section). For convenience, in Fig. 5 (a) we schematically re-

produce the transitions participating near III where the first transmon is below the second one, and the current of the resonance point where $\omega_1 = \omega_2 + \alpha_2/2$ is shown with a dashed gray line. Next, in Fig. 5 (b) we plot the level structure of the SAM at the resonance point. The single-photon drive by $\hat{H}_d^{(1)}$ detuned by Δ_1 from ω_1 is shown with orange ellipses. The much weaker two-photon drive by $\hat{H}_d^{(2)}$ is not shown yet because it does not alter the structure of the energy levels. Since we know from the numerical simulations that the third level of the first transmon is not necessary to observe the splitting, $|20\rangle$ is shown transparent, and states $|21\rangle$, $|22\rangle$ are not shown.

The next step is to view the system in the frame rotating with the first transmon and then move to the dressed picture similarly to Appendix B. Now, the first transmon splitting equals $\Omega_1^R = \sqrt{\Omega_1^2 + \Delta_1^2}$, and its new eigenstates (dressed states) are denoted as $|a\rangle$ and $|b\rangle$. Meanwhile, the second transmon subspace is not altered. The corresponding level system in the rotating frame before and after modification by the drive is shown in Fig. 5 (c).

Finally, in Fig. 5 (d) we demonstrate possible two-photon transitions between the dressed states induced by the second transmon driving $\hat{H}_d^{(2)}$. In the left part of the panel, one can find the unmodified two-photon transition 02/2 at ω_1 and two sidebands at $\omega_1 \pm \Omega_1^R/2$. This picture finally explains the ob-

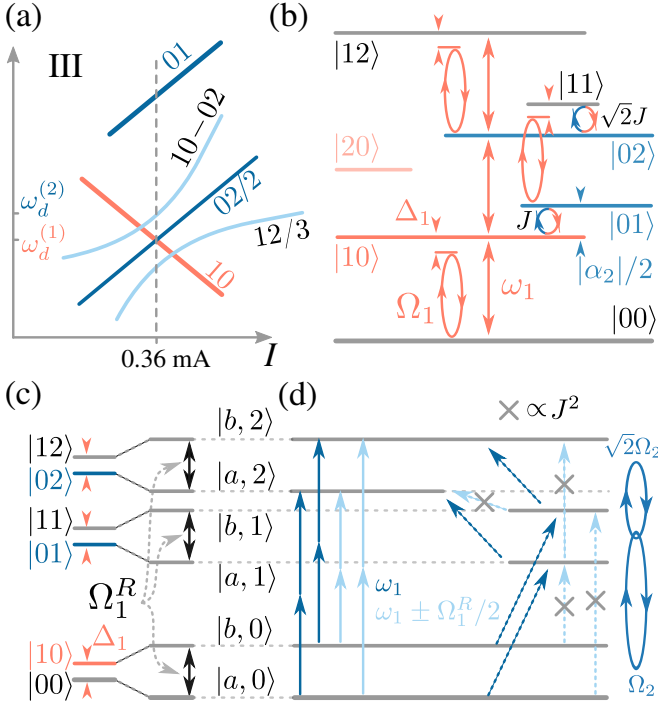


FIG. 5. (a) Schematic of the transition frequencies near III (not to scale). Resonant point is marked by a dashed gray line. Here we assume that each transmon is driven at its own frequency. (b) System energy levels at the resonant point; the first transmon drive at a small detuning Δ_1 from ω_1 is shown as orange ellipses. The second transmon driving is not shown here. Action of \hat{H}_{int} in RWA is depicted as orange-blue circles. (c) In the frame rotating with $\hat{H}_d^{(1)}$, states $|0j\rangle, |1j\rangle$ become nearly degenerate ($\omega_1 \rightarrow \Delta_1$). Dressing increases this splitting to Ω_1^R . (d) Transitions in the dressed system induced by $\hat{H}_d^{(2)}$ (coupled level subspaces are shown with blue ellipses). In the left part of the panel, all possible two-photon transitions near ω_1 are depicted: the blue transitions are not shifted in frequency, the light blue ones are shifted by $\pm\Omega_1^R/2$. In the right part, some of the contributing trajectories are depicted; gray crosses show transitions that are forbidden without the coupling J .

served triplet transition of feature III. The right part describes the mechanism of these two-photon processes through virtual excitations of the intermediate states. From here it becomes obvious that without the transmon-transmon interaction the sideband transitions are forbidden due the selection rule: $\langle a, j | \hat{1} \otimes \hat{H}_d^{(2)} | b, j+1 \rangle = 0$ since $\langle a | b \rangle = 0$. However, we will show that they become allowed in the second order in J when the coupling is turned on.

Now, we will repeat this reasoning quantitatively. We start from the initial Hamiltonian, Eq. 3. To move to the rotating frame with Eq. 5 and apply the RWA, we use the following operator:

$$R = \exp \left[-it \omega_d^{(1)} (b^\dagger b + c^\dagger c) \right]. \quad (11)$$

Note that now we rotate both transmon subspaces simultaneously in contrast to what is shown in Fig. 5 because below it

will be convenient to have time-independent \hat{H}_{int} . Now,

$$\begin{aligned} \omega_{1,2} &\rightarrow \Delta_{1,2} = \omega_{1,2} - \omega_d^{(1)}, \\ \hat{H}_{int} &\rightarrow \hbar J [\hat{\sigma}_+ \hat{c} + \hat{\sigma}_- \hat{c}^\dagger], \\ \hat{H}_d^{(1)} &\rightarrow \frac{\hbar \Omega_1}{2} \hat{\sigma}_x, \quad \hat{H}_d^{(2)} \rightarrow \frac{\hbar \Omega_2}{2} (\hat{c} e^{i\delta t} + \hat{c}^\dagger e^{-i\delta t}), \end{aligned} \quad (12)$$

where $\delta = \omega_d^{(2)} - \omega_d^{(1)}$.

Since $\hat{H}_d^{(1)}$ is now time-independent, we can move to the dressed basis by applying a transformation \hat{S} which diagonalizes the first transmon. After that, the Hamiltonian may be split into three parts

$$\begin{aligned} \hat{H}^D / \hbar &= \left[\frac{\Delta_1}{2} \hat{1} - \frac{\Omega_1^R}{2} \hat{\sigma}_z \right] + \Delta_2 \hat{b}^\dagger \hat{b} + \frac{1}{2} \alpha_2 \hat{b}^\dagger \hat{b} (\hat{b}^\dagger \hat{b} - 1), \\ \hat{V}_J &= \hat{S}^\dagger \hat{H}_{int} \hat{S}, \\ \hat{V}_I(t) &= \hat{S}^\dagger \hat{H}_d^{(2)} \hat{S} \equiv \hat{H}_d^{(2)}. \end{aligned} \quad (13)$$

The first part is diagonal, and the remaining two will be treated as perturbations. To simplify further calculations, we consider the point where $\Delta_1 = 0$ and $\Delta_2 = |\alpha_2|/2$. In these conditions, \hat{H}^D becomes degenerate as can be seen in Eq. C6 of Appendix C. Using the degenerate perturbation theory for \hat{V}_J summarized therein, we find the first-order corrected wave functions of $\hat{H}^D + \hat{V}_J$, labeled $|k\rangle$, $k = 1..6$. We find the mean relative element-wise error of around 3% between numerically obtained eigenvectors and perturbative ones for our experimental parameters.

The time-dependent perturbation theory that we use to calculate the transition rates of the two-photon processes stimulated by \hat{V}_I is reviewed in Appendix D. Using the corrected eigenstates $|k\rangle$ and neglecting small terms, we obtain the following expressions for the transition rates per unit time [51]:

$$\begin{aligned} R_{2 \rightarrow 5}^{(2)} &\approx \pi \Omega_2^4 \frac{16J^4 (3\alpha^2 + 7\Omega_1^2)^2}{\alpha^{10}}, \\ R_{1 \rightarrow 6}^{(2)} &\approx \pi \Omega_2^4 \frac{4J^4 (5\alpha - 3\Omega_1)^2}{\alpha^8}, \end{aligned} \quad (14)$$

when $|\alpha_2| \gg \Omega_1, \Omega_2, J$ which is a good approximation for our setup. Taylor expansion here leads to errors of less than 0.5%. From Eq. 14 follows that the sideband transitions are prohibited without the interaction in the SAM ($J = 0$), and the extra avoided crossings will not be observed.

The above reasoning can be repeated for feature II without modification because it is only different from III in the ordering of the transmons.

b. Feature I. Finally, we discuss the remaining Roman-numbered effect. In the case when $\Omega_2 \gg \Omega_1$ (the second transmon is dressed) the splitting has the shape shown in Fig. 6 (a). For the opposite case ($\Omega_1 \gg \Omega_2$), the logic is similar.

As one can see from Fig. 4, near the 01, 10 intersection only the two-photon transition 11/2 is affected and deviates from the unperturbed spectrum while the spectral lines 01, 10 do not shift (even though the avoided crossing between them vanishes). Similarly to II and III, in the frame rotating with

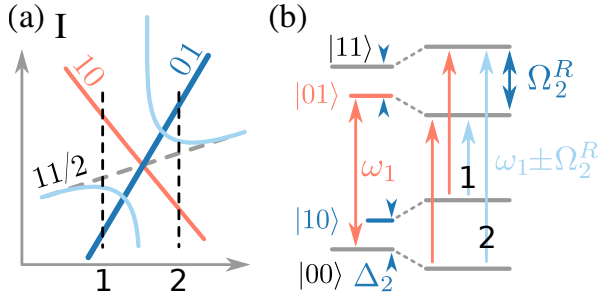


FIG. 6. Feature I for the case of $\Omega_2 \gg \Omega_1$. (a) Schematic of the spectral lines near I (the avoided crossing between 01 and 10 is not shown). Compare to Fig. 4, middle row. (b) Transitions between dressed states in the frame rotating with the second transmon. Two sideband transitions (light blue) appear at frequencies $\omega_1 \pm \Omega_2^R$; however, only one of them may be observed at each side of the intersection for a monochromatic signal (see Section III D).

the second transmon it turns into two different single-photon transitions for $\hat{H}_d^{(1)}$ located at $\omega_1 \pm \Omega_2^R$, see Fig. 6 (b). We will show below that in the experiment with a single excitation frequency, it is not possible to observe both transitions simultaneously. This is also clear from Fig. 4 where only one spectral line is present to the left and one to the right from the 01, 10 intersection.

D. Self-consistent equations for the I, II, III

In the previous section, we have assumed that the transmons are driven independently at two different frequencies. In this section, we will discuss the realistic case when only a single frequency ω_d is sent at the SAM.

a. Features II, III. We start again with feature III. As before, from Fig. 5 (d) we know that at the intersection the sideband transitions are formed by the two two-photon processes with $\hat{H}_d^{(2)}$. But, on the other hand, from the unperturbed solution we know that in the laboratory frame these two sideband transitions beyond the avoided crossing in III become 10 – 02 (one-photon) and 12/3 (three-photon). This means that there should be a smooth transformation between these one-, two- and three-photon processes when the system approaches the resonant point where $\alpha_2 + 2\omega_2 = 2\omega_1$. Let us consider hypothetical two-photon transitions $(10 - 02)/2$ and $12/2$. In the frame rotating with the first transmon like in Fig. 5 (c) when $\Omega_1 = 0$, their frequencies are

$$\omega_{(10-02)/2} = (\alpha_2 + 2\omega_2 - \Delta_1)/2, \quad (15)$$

$$\omega_{12/2} = (\alpha_2 + 2\omega_2 + \Delta_1)/2. \quad (16)$$

When the first transmon becomes dressed by $\Omega_1 \neq 0$, its splitting Δ_1 changes to $\Omega_1^R = \sqrt{\Omega_1^2 + (\omega_1 - \omega_d)^2}$. Substituting Ω_1^R instead of Δ_1 into the equations above we note that $\omega_{(10-02)/2}$ and $\omega_{12/2}$ are now exactly equal to the two-photon sideband frequencies $\omega_1 \pm \Omega_1^R/2$ established in the previous section. Therefore, it is logical to use them to model the splitting behavior beyond the resonant point.

Since we are dressing the energy levels by $\hat{H}_d^{(1)}$ and probing two-photon transitions between them with $\hat{H}_d^{(2)}$ both at ω_d , self-consistent equations have to be solved to find at which detuning the sideband spectral lines will appear:

$$\begin{aligned} \omega_{(10-02)/2} &= \omega_d, \\ \omega_{12/2} &= \omega_d, \end{aligned} \quad (17)$$

where the left hand side for each equation is calculated according to Eq. 15 and Eq. 16, respectively.

First, we analyse the solution of Eq. 17 in the case of no driving, $\Omega_1 = 0$. Both equations yield two identical answers for ω_d due to the fact that $\Omega_1^R = |\omega_1 - \omega_d|$ in this case. One can identify them as the frequencies of the three-photon 12/3 and the single-photon 10 – 02 transitions in the laboratory frame:

$$\omega_d^{(III,0)} = \begin{cases} (\alpha_2 + 2\omega_2 + \omega_1)/3, \\ \alpha_2 + 2\omega_2 - \omega_1. \end{cases} \quad (18)$$

Thus is a correct solution for the edge case since with no dressing, these transitions just intersect without an avoided crossing.

Next, for the general case of non-zero driving, $\Omega_1 \neq 0$, we obtain again two identical pairs of solutions:

$$\begin{aligned} \omega_d^{(III,\pm)} &= \frac{2\alpha_2}{3} + \frac{4\omega_2}{3} - \frac{\omega_1}{3} \\ &\pm \frac{\sqrt{3\Omega_1^2 + (\alpha_2 + 2(\omega_2 - \omega_1))^2}}{3}. \end{aligned} \quad (19)$$

These new curves do not intersect at any point, correctly reproducing the behavior observed in the experiment and in the numerical data and forming two branches of an anticrossing. The minimal splitting is found at the resonant point and equals $\frac{2\sqrt{3}}{3}\Omega_1$. A similar result can be produced for the feature II just by swapping the transmons; in that case, the splitting will be $\frac{2\sqrt{3}}{3}\Omega_2$.

We find excellent agreement between the self-consistent solution Eq. 19 and both the experimental and simulated data as can be seen in Fig. 3. To plot the model curves, we have approximated the $\omega_{1,2}(\Phi_e)$ transitions by linear functions and substituted them in Eq. 19. α_1 is known from spectroscopy leaving only Ω_2 to be found by fitting. We have repeated this approximation for a range of microwave powers to confirm the linear dependence of the splitting on the excitation amplitude (see Fig. 3 (c)).

The deviation of the upper branch from the data (see Fig. 3, dotted lines) is expected and caused by the avoided crossing marked as the secondary feature 3; it could be taken into account by modifying correspondingly Eq. 16. The small discrepancy between the experimental and simulated data in the upper branch is caused by a slight elevation of the lower sweet spot of the first transmon moving the avoided crossing 3 closer to the feature II in the second cooldown.

b. Feature I. Feature I may be explained using the same dressing model. Looking at Fig. 6 for the case $\Omega_2 \gg \Omega_1$, we can write another pair of self-consistent equations:

$$\omega_1 \pm \Omega_2^R = \omega_d^{(I,-)}. \quad (20)$$

Substituting $\Omega_2^R = \sqrt{\Omega_2^2 + (\omega_2 - \omega_d^{(I,-)})^2}$, one can find that this system has a single solution

$$\omega_d^{(I,-)} = \frac{\omega_1 + \omega_2}{2} - \frac{\Omega_2^2}{2(\omega_1 - \omega_2)}, \quad (21)$$

which turns into the frequency of 11/2 in the laboratory frame when Ω_2 is zero. When Ω_2 is non-zero, the solution near the point $\omega_1 \approx \omega_2$ is a hyperbolic curve. However, in reality we do not observe the asymptotically vertical parts since the model becomes invalid when $|\omega_1 - \omega_2| \leq J$ due to the finite coupling between the transmons, and thus the avoided crossing between 01 and 10. Since ω_1 and ω_2 never reach each other, the denominator in (21) is limited from below and there is no actual divergence.

When $\Omega_1 \gg \Omega_2$, besides replacing $\Omega_2 \rightarrow \Omega_1$, one have to change the sign before the hyperbolic part to obtain the corresponding solution:

$$\omega_d^{(I,+)} = \frac{\omega_1 + \omega_2}{2} + \frac{\Omega_1^2}{2(\omega_1 - \omega_2)}, \quad (22)$$

yielding the reversed shape of the splitting.

Continuing this logic, we can write down the resonance condition in the doubly-rotating frame when both transmons are dressed simultaneously:

$$\Omega_1^R \pm \Omega_2^R = 0. \quad (23)$$

Solving it for ω_d , we obtain the generalization of Eq. 21 and Eq. 22:

$$\omega_d^I = \frac{\omega_1 + \omega_2}{2} + \frac{\Omega_1^2 - \Omega_2^2}{2(\omega_1 - \omega_2)} \quad (24)$$

Eq. 24 is used to plot the black dashed curves in Fig. 4 taking the $\Omega_{1,2}$ values from the known simulation parameters shown therein. The frequencies $\omega_{1,2}$ are extracted from the fits of the spectral lines 01 and 10. We again find good agreement between the model and the simulated data.

IV. DISCUSSION

We have performed spectroscopic measurements of an isolated diatomic superconducting artificial molecule in the regime of strong interaction with classical light. Using joint dispersive readout to directly access the population of the SAM eigenstates, we have located several anomalies in the spectrum not explained by the unperturbed model of the system. Finding numerically the steady state of the SAM interacting with the classical drive, we have reproduced the experimentally discovered effects and attributed them to an altered version of the well-known Autler-Townes effect.

In contrast to the standard A-T effect, where there are two laser beams of different frequencies and powers, in our case, there is only a single tone interacting with the system. Therefore, it has to be both the coupler tone and the probe tone at the same time. However, since there are two components in

the driving operator (one for each transmon), the separation between the coupler and the probe is still possible and occurs both in the Hilbert space and in the number of photons involved rather than in frequency and amplitude. The effectively weak driving limit for the probe part is achieved when it stimulates a two-photon transition while the coupler part is resonant with a single-photon one being strong enough to dress the system. To predict the frequencies of the sideband transitions that can appear for such A-T-like processes and to model the experimentally observed splittings induced by the same field that probes them, we have built several self-consistent models in rotating frame and found a good agreement between the model, the experiment, and the numerical simulation. Interestingly, no new spectral lines appear when the system is tuned to the parameters where these A-T-like processes can occur. Instead, for example, one can see how the already present spectral lines 12/3 (three-photon) and 10-02 (single photon) smoothly morph to an additional avoided crossing of a non-standard size of $\frac{2\sqrt{3}}{3}\Omega_1$.

Another A-T-like effect may occur when both components of the driving operator are in the single-photon regime. Now, both transmons are dressed and probed simultaneously. We find that in this case the 11/2 transition frequency is altered. When the SAAs are being tuned into resonance, this spectral line is being split into two hyperbolic curves. However, unlike the case of a standard avoided crossing, the doublet transition is never observed. The shape of this apparent splitting and its visibility depends qualitatively on the relation between the driving amplitudes; for instance, if they are equal, the splitting does not appear at all. For our sample, we have a fixed ratio of approximately two between Ω_1 and Ω_2 which still allows us to distinguish this effect experimentally. Notably, light dressing affects the frequency of the 11/2 transition even far from the 01, 10 intersection. This means that a fast bSWAP gate should be performed at a different frequency than predicted by the unperturbed Hamiltonian if there is an asymmetry in the driving amplitudes $\Omega_{1,2}$.

Interestingly, the self-consistent models for the observed effects imply that multi-photon processes may smoothly change their order. For example, for features II and III, we observe a continuous transformation of a three-photon and a single-photon processes to the second order in Eq. 17, and of a two-photon transition to a zero-photon in Eq. 23. One could quantify this effect by evaluating the transition linewidths and measuring their power dependence for different coil currents.

Overall, irradiating an individual diatomic artificial molecule with intense light calls forth a plethora of effects that may be used to extend the validity of the well-known light-dressing models. These effects are much easier to find in human-made quantum devices than in natural coupled systems due to higher overall controllability and addressability of their parts. The relative ease in attaining the excitation powers that cause multiphoton transitions promises even more complex dynamics in multi-atom systems. We are looking forward to investigating strong interaction with light in larger artificial structures such as one- and two-dimensional arrays of SAA.

V. ACKNOWLEDGEMENTS

We gratefully acknowledge valuable discussions with I.S. Besedin, V.V. Ryazanov, and A.V. Ustinov. The experimental investigation was conducted with the support of Russian Science Foundation, Grant No. 16-12-00070. Numerical simulations were supported by the Russian Science Foundation (contract no. 16-12-00095). The theoretical work was supported by Ministry of Science and Higher Education of Russian Federation in the framework of Increase Competitiveness Program of the NUST MISIS (contract no. K2-2017-081). Devices/Samples were fabricated at the BMSTU Nanofabrication Facility (Functional Micro/Nanosystems, FMNS REC, ID 74300)

Appendix A: Full circuit model

In this section, we substantiate our use of the simplified model in Eq. 3 and compare our experiment with previous works. From the scheme in Fig. 1 (b) and from [41] we can conclude, that we have two types of interaction between SAAs and that our choice for \hat{H}_{int} is valid. The only difference is in the representation of the charge operator \hat{n} which we choose to be proportional to $\hat{b}^\dagger + \hat{b}$ instead of $i(\hat{b}^\dagger - \hat{b})$ which is a question of the basis choice (the linear oscillator basis or the transmon eigenbasis). The flipped sign before the counter-RWA terms is important only for the coupling to the resonator. However, it can be corrected by an altered Schrieffer-Wolff transformation leading to identical final results. The symmetries of the drive and the coupling operator stay unchanged with this approach. Having established the correctness of our simplified model, we can proceed and calculate the coupling strengths.

The first one, J_{12} , is caused by the direct capacitive coupling, and following [41] we see that:

$$J_{12} = \frac{1}{2}(1 + \eta) \frac{C_{12}}{\sqrt{C_1 C_2}} \sqrt{\omega_1 \omega_2},$$

where C_{12} is the mutual capacitance between the transmon islands, $C_{1,2}$ are their capacitances to the ground, and $\omega_{1,2}$ are defined as in the main text. The coefficient η is around $6 \cdot 10^{-2}$ for our parameters as will be shown later.

The second coupling mechanism is via the multimode quantum bus, similar to [27, 31]. However, the models used in these papers can now be improved using [41] (counter-RWA terms must be taken into account for higher modes that are in the strong dispersive regime) and [52, 53] that have solved the divergence problems and found rigorously the effective cut-off frequency f_{max} that we will employ. For our case, f_{max} can be calculated using the equivalent capacitance of the network at the open end of the $\lambda/4$ resonator:

$$C_{eff} \approx C_{claw} + (C_{g1}^{-1} + C_1^{-1})^{-1} + (C_{g2}^{-1} + C_2^{-1})^{-1},$$

where $C_{g1,g2}$ are the capacitances between the transmons and the resonator, C_{claw} is the direct capacitance of the claw coupler to the ground plane, and C_{12} and capacitances to the drive

antenna are neglected. Now, to find f_{max} we need to solve the equation

$$\left| \frac{1}{i2\pi f_{max} C_{eff}} \right| = |Z_{res}| \approx 50 \Omega$$

which marks the frequency above which the capacitive impedance at the end of the resonator will become small enough (comparable to its wave impedance Z_{res}) to effectively change the boundary condition there to a short, turning off the electric field and thus the capacitive coupling of the higher-frequency modes to the transmons.

Next, we use the expression for the coupling through the j^{th} mode with the frequency ω_j^r based on [41] with the counter-RWA terms:

$$J_{bus}^{(j)} \approx \frac{g_1^{(j)} g_2^{(j)}}{2} \left(\frac{1}{\Delta_1^{(j)}} + \frac{1}{\Delta_2^{(j)}} - \frac{1}{\Sigma_1^{(j)}} - \frac{1}{\Sigma_2^{(j)}} \right), \quad (\text{A1})$$

where $\Delta_{1,2}^{(j)} = \omega_{1,2} - \omega_j^r < 0 \forall j$, $\Sigma_{1,2}^{(j)} = \omega_{1,2} + \omega_j^r$, and

$$g_{1,2}^{(j)} = \frac{1}{2} \frac{C_{g1,g2}}{\sqrt{C_{1,2} C_r}} \sqrt{\omega_{1,2} \omega_j^r}, \quad (\text{A2})$$

where the effective mode capacitance $C_r = C_r' l_r / 2 + C_{claw}$ does not depend on j [41, 54]. $C_r' = 160$ fF/mm being the per-unit-length capacitance may be calculated for a CPW (center width of $7 \mu\text{m}$, gap of $4 \mu\text{m}$) with standard means (here and below we take the substrate ϵ to be 11.45 [55]); $l_r = 3.477$ mm is the resonator length without the claw. C_{claw} may be found from EM simulations or from the equation determining the observed resonator frequency:

$$\omega_0 = \frac{1}{\sqrt{L_r^{(0)} (1 + \alpha) (C_r' l_r / 2 + C_{claw})}}, \quad (\text{A3})$$

where $\alpha = 0.14$ is the kinetic inductance contribution determined using two test resonators without claws and $L_r^{(0)} = 8L_r' l_r / \pi^2$ is the geometric equivalent inductance of the fundamental mode, $L_r' = 0.4$ nH/mm. From EM simulation, we find $C_{claw} = 64$ fF; however, from Eq. A3 we obtain $C_{claw} = 53$ fF. We are unable to explain why the difference is so significant, even though we could successfully describe the frequencies of all 4 different resonators on the chip (two with transmon pairs and claws, at 6.840 and 7.340 GHz, and two test ones, at 7.700 and 7.800 GHz) up to MHz accuracy with Eq. A3 while fitting only α and C_{claw} . Below we will use the smaller value for C_{claw} determined from the experimental data.

Knowing $C_r = 337$ fF, the capacitances $C_{g1,g2}$ may be determined with high accuracy by fitting the fundamental mode frequency dependence on the flux using Eq. A2 when the transmon parameters are known (see also [56]). $C_{1,2}$ can be extracted from the experimental anharmonicity using the equation

$$-\hbar\alpha = E_C^{1,2} = \frac{e^2}{2C_{1,2}},$$

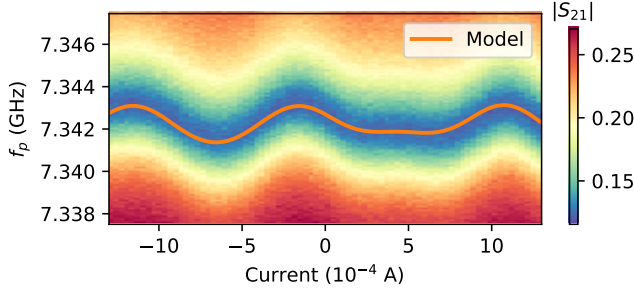


FIG. 7. Determining the coupling strength via the resonator spectroscopy (external coil current is swept, flux bias lines turned off, transmission amplitude is shown). The transmon parameters $E_{J,\Sigma}^{(1,2)}$, $E_C^{(1,2)}$, $d^{(1,2)}$ are fixed to the values from Section II A, and the bare cavity frequency, current sweet spots, current periods and coupling capacitance $C_g = C_{g1} = C_{g2}$ are the fitting parameters. The orange curve shows the theoretical prediction for the optimal values: $\omega_0/2\pi = 7.340$ GHz, sweet spots at -1.2 and 0.45 mA, periods of 1.15 and 0.74 mA, $C_g = 2.5$ fF.

which yields $C_{1,2} \approx 88$ fF (we use here the renormalized $E_C^{1,2}$ from [53], Eq. 6). The fit is shown in Fig. 7, which yields the capacitances $C_{g1,g2}$ of 2.5 fF each, which agrees reasonably well with the value of 2.3 fF that we have obtained from EM simulation. We have checked that the sweet spots found this way agree with an independent direct SAM spectroscopy similar to Fig. 2 (a). The discrepancy in $C_{g1,g2}$ probably arises from the real configuration of the ground electrode enclosing the chip in the sample holder which we do not include in the simulation. Similarly, we obtain simulated $C_{1,2}$ to be only 80 fF. This problem also hampers the accuracy of the calculated C_{12} which unfortunately can not be found independently in this experiment.

In overall, the total interaction

$$J = J_{12} + \sum_{j=0}^{j_{max}} J_{bus}^{(j)},$$

where $j_{max} : \omega_j^r \approx 2\pi f_{max}$. For our configuration, the first term is positive, and the second is negative. Note that in contrast to [31], the contribution from every mode is of the same negative sign since the transmons are located at the same resonator end and are below all modes in frequency. Below, we calculate the value of J at $\omega_{1,2} \approx 5.3$ GHz where we can determine its value experimentally from the size of the avoided crossing.

For the parameters $C_{1,2} = 88$ fF, $C_{g1,g2} = 2.5$ fF, $C_{claw} = 53$ fF we find that $C_{eff} \approx 59$ fF and $f_{max} \approx 55$ GHz. Since $\omega_j^r = (2j+1)\omega_0^r$, $\omega_0^r/2\pi \approx 7.3$ GHz, and $\omega_3^r/2\pi \approx 51$ GHz $\approx f_{max}$, we only need to include 4 terms for the multimode virtual interaction between the transmon. We note that this very low cut-off is due to the large direct capacitance of the claw to the ground.

Having established the required cut-off, we can evaluate the multimode contribution. In Fig. 8, we show its value depending on the number of included modes with and without RWA. As one can see, the cumulative value at the cut-off is approximately -3 MHz for the non-RWA case and -2 MHz within

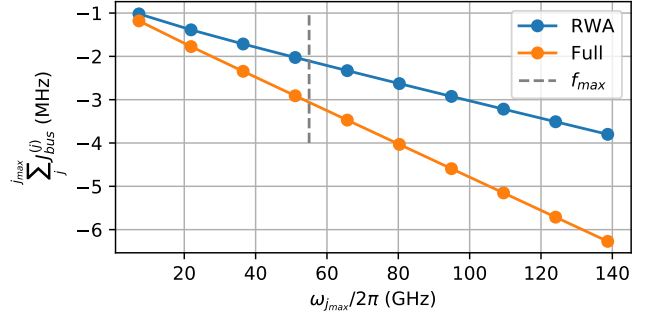


FIG. 8. Multimode coupling vs $\omega_{j_{max}}$. Blue points show the RWA result (without the $\Sigma_{1,2}^{(j)}$ terms) and orange show the full calculation. Gray dashed line shows the calculated cut-off frequency of 55 GHz. The parameters for the calculation: $\omega_{1,2}/2\pi = 5.3$ GHz, $\omega_0/2\pi = 7.3$ GHz, $C_{1,2} = 88$ fF, $C_r = 337$ fF, $C_{g1,g2} = 2.5$ fF giving $g_{1,2}^{(0)}/2\pi = 45$ MHz.

RWA. For higher cut-off frequencies, the ratio between RWA and full solution tends to 2, since $\Sigma_{1,2}^{(j)} \approx -\Delta_{1,2}^{(j)}$ there.

Next, we find the direct coupling constant. As we have already mentioned, the capacitance C_{12} can only be determined in a FEM simulation; however, it depends on the configuration of the ground plane stronger than $C_{g1,g2}$ and $C_{1,2}$ and thus is less accurately determined. The root of this is in the large size of the transmon island electrodes comparable to the substrate thickness of 0.4 mm. We use a sample holder with a machined cavity under the chip, and for a realistic FEM model, we obtain $C_{12} = 0.34$ fF. This yields $\eta = C_{g1}C_{g2}/C_{12}C_r = .059$, and the resulting direct coupling $J_{12} \approx 11$ MHz.

Finally, adding both contributions, we find $J \approx 8$ MHz which agrees reasonably well with the experimental value of 8.69 MHz. The positive sign of the coupling is consistent with the location of the dark state in the lower branch of the avoided crossing between 01 and 10 in the experimental data which we have established in a separate measurement [31]. Despite the uncertainty in J_{12} , this result confirms that the cut-off frequency for cQED with a transmission line resonator should be calculated regarding the effective capacitance at its end and may be quite low. However, our accuracy is not enough to demonstrate confidently the necessity of the counter-RWA terms. It is notable that, in contrast to this work, [31] describes the experimental data within RWA, but does not adopt a possibly lower cut-off for their capacitances, so a separate study may be required to clarify the importance of the counter-rotating terms. Additionally, it would be interesting to compare the results with [57], presenting a classical approach to the problem, suitable for low-anharmonicity circuits.

To end this subsection, we would like to comment on the possible error sources in our reasoning. First, a more rigorous cut-off free analysis similar to [53] should be conducted for our circuit to substantiate the use of the cut-off and find the renormalized Hamiltonian parameters. It would be possible if it is possible to find analytically the inverse capacitance matrix of the system, as was done in [53]. Second, the use of the $(\hat{b}^\dagger + \hat{b})(\hat{c}^\dagger + \hat{c})$ form for the coupling via the bus is not ab-

solutely rigorous, because for higher transmon levels Eq. A1 will include slightly different $\Delta_{1,2}^{(j)}$ and $\Sigma_{1,2}^{(j)}$ due to the non-zero α [58].

Appendix B: Standard Autler-Townes effect for a three-level Ξ atom

The underlying cause of the A-T effect is the dressing of the atomic levels by strong EM radiation. There are two equivalent mathematical models to describe it depending on whether the light is classical or quantized [8].

a. Classical derivation. In the classical case, the mathematical description goes as follows. The $|0\rangle \rightarrow |1\rangle$ transition of frequency ω_{01} in a three-level system is driven strongly with an amplitude Ω_c at a detuning Δ (the *coupler tone*). Additionally, weak radiation at ω_p and of amplitude Ω_p is sent at the $|1\rangle \rightarrow |2\rangle$, transition, of frequency ω_{12} (the *probe tone*). This is illustrated in Fig. 9 (a). The Hamiltonian for this driven system reads:

$$\hat{H}_0/\hbar = \begin{bmatrix} 0 & \Omega_c \cos(\omega_{01} - \Delta)t & 0 \\ \Omega_c \cos(\omega_{01} - \Delta)t & \omega_{01} & \Omega_p \cos \omega_p t \\ 0 & \Omega_p \cos \omega_p t & \omega_{02} \end{bmatrix},$$

where $\omega_{02} = \omega_{01} + \omega_{12}$.

Next, we move to the rotating frame by using an operator

$$\hat{R} = \begin{bmatrix} 1 & 0 & 0 \\ 0 & e^{-i(\omega_{01} - \Delta)t} & 0 \\ 0 & 0 & e^{-i(\omega_{01} - \Delta)t} \end{bmatrix}.$$

Note here that the state $|2\rangle$ is also rotated: this is convenient to preserve the frequency of the probe field. The new Hamiltonian is calculated as follows: $\hat{H}_1 = \hat{R}^\dagger \hat{H}_0 \hat{R} - i\hat{R}^\dagger \partial_t \hat{R}$. The level

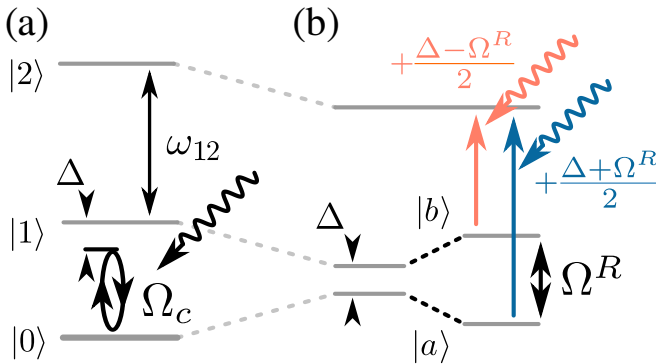


FIG. 9. Illustrating the A-T splitting by the classical driving in the rotating frame. (a) A three-level system is driven strongly by the coupler tone of amplitude Ω_c at frequency $\omega_c = \omega_{01} - \Delta$. (b) In the frame rotating with the drive, the $|0\rangle \rightarrow |1\rangle$ transition frequency changes to Δ . However, when the RWA is applied and the Hamiltonian is re-diagonalized, the splitting between two lowest levels (dressed states $|a\rangle$ and $|b\rangle$) becomes $\hbar\Omega^R$. Now, a doublet transition from these levels to the state $|2\rangle$ at frequencies $\omega_{12} + (\Delta \pm \Omega^R)/2$ may be observed.

structure without driving is shown in the left part of Fig. 9 (b). Applying the RWA, we obtain:

$$\hat{H}_1/\hbar = \begin{bmatrix} 0 & \Omega_c/2 & 0 \\ \Omega_c/2 & \Delta & \Omega_p e^{i\omega_p t}/2 \\ 0 & \Omega_p e^{-i\omega_p t}/2 & \omega_{02} - \omega_{01} + \Delta \end{bmatrix}.$$

Next, moving to the basis where the upper left 2x2 corner is diagonal (the right part of Fig. 9 (b)), we obtain:

$$\hat{H}_3/\hbar = \begin{bmatrix} \frac{\Delta}{2} - \frac{\sqrt{\Delta^2 + \Omega_c^2}}{2} & 0 & \frac{\Omega_p e^{i\omega_p t}}{2} \sin(\theta) \\ 0 & \frac{\Delta}{2} + \frac{\sqrt{\Delta^2 + \Omega_c^2}}{2} & \frac{\Omega_p e^{i\omega_p t}}{2} \cos(\theta) \\ \frac{\Omega_p e^{-i\omega_p t}}{2} \sin(\theta) & \frac{\Omega_p e^{-i\omega_p t}}{2} \cos(\theta) & \omega_{12} + \Delta \end{bmatrix}.$$

One may see that the resonant conditions for the probe drive are now $\omega_p = \omega_{12} + (\Delta \pm \Omega^R)/2$, where $\Omega^R = \sqrt{\Omega_c^2 + \Delta^2}$, $\omega_{12} = \omega_{02} - \omega_{01}$, and its amplitude is renormalized by an angle θ , $\tan 2\theta = -\Omega_c/\Delta$.

b. Quantum derivation. For a fully quantum interpretation, the incident radiation at $\omega_{01} - \Delta$ is modelled as a single-mode quantum oscillator which is then coupled to the $|0\rangle \rightarrow |1\rangle$ transition. The Hamiltonian for the compound system reads:

$$\hat{H}_0/\hbar = \omega_{01} |1\rangle \langle 1| + \omega_{02} |2\rangle \langle 2| + (\omega_{01} - \Delta) \hat{a}^\dagger \hat{a} + g(\hat{a}^\dagger + \hat{a}) \otimes (|1\rangle \langle 0| + |0\rangle \langle 1|),$$

where g is the coupling strength and a is the photon annihilation operator. After moving to the rotating frame with $\hat{R} = \exp[i(\omega_{01} - \Delta)(\hat{a}^\dagger \hat{a} + |1\rangle \langle 1| + |2\rangle \langle 2|)]$ and applying the RWA, the Hamiltonian transforms into

$$\hat{H}_1/\hbar = \Delta |1\rangle \langle 1| + (\omega_{12} + \Delta) |2\rangle \langle 2| + g[\hat{a}^\dagger \otimes |0\rangle \langle 1| + \hat{a} \otimes |1\rangle \langle 0|]. \quad (\text{B1})$$

Now, presume that the resonator is in a coherent state $|\alpha\rangle$ with $\langle N \rangle = \alpha^2$ photons (it is time-independent in the rotating frame). Therefore, after tracing out the resonator subspace, from the interaction term we will obtain again the classical driving term $\Omega_c (|0\rangle \langle 1| + |1\rangle \langle 0|)$, where $\Omega_c = 2g\sqrt{\langle N \rangle}$ in correspondence with the previous approach. The following steps completely reproduce the classical case if we add the probe tone Ω_p to the last equation.

Appendix C: Degenerate perturbation theory

Since the Hamiltonian in the dressed basis is a useful illustration for Fig. 5, we provide it below in Eq. C6 for the case $\Delta_1 = 0$, $\delta = \omega_d^{(2)} - \omega_d^{(1)} = \omega_d^{(2)} - \omega_1$. In the resonant case $2\Delta_2 + \alpha_2 = 0$, i.e. when the frame of the second transmon is rotated at its two-photon transition frequency (as in III), there is a degeneracy between states $|a, 0\rangle, |a, 2\rangle$ and $|b, 0\rangle, |b, 2\rangle$, while $|a, 1\rangle, |b, 1\rangle$ are detuned from them by $|\alpha_2|/2$.

Note that in the dressed basis \hat{H}_{int} that we treat as a perturbation has a sub- and super-diagonal block form and couples all the states $|a, j\rangle, |a, j+1\rangle$ and $|b, j\rangle, |b, j+1\rangle$.

The degenerate perturbation theory requires first of all to choose zero-order state vectors $|N^0\rangle$ from a degenerate subspace. The choice is arbitrary at the first glance because any linear combination of basis vectors $|n\rangle$ from this subspace will satisfy the unperturbed Schrödinger equation. However, if we demand the *change* of $|N^0\rangle$ to be small under the perturbation \hat{V} , they become determined and are given by diagonalization of \hat{V} in the degenerate subspace. Unfortunately, all matrix elements of $\hat{V} = \hat{V}_J$ are zero in both our degenerate subspaces, so technically any choice of zero-order states will diagonalize it. In other words, the degeneracy is not lifted in the first-order, and thus we have [59] to diagonalize the matrix

$$M_{nn'} = \sum_m \frac{V_{nm}V_{mn'}}{E_n - E_m}. \quad (\text{C1})$$

Here, $|n\rangle$ and $|n'\rangle$ are the basis states from the degenerate subspace with energy E_n , and $V_{mn} = \langle m|\hat{V}|n\rangle$. The sum is over all other zero-order states $|m\rangle$ outside the degenerate subspace.

For example, in our case for one of the degenerate subspaces ($E_n^0 = -\Omega_1/2$, $\hat{V} = \hat{V}_J$) we obtain the following matrix:

$$M_{15} = \begin{array}{l} |a,0\rangle \\ |a,2\rangle \end{array} \begin{array}{l} \begin{array}{l} |a,0\rangle \\ |a,2\rangle \end{array} \left[\begin{array}{cc} \frac{J^2(\Omega_1 - \alpha_2)}{\alpha_2(2\Omega_1 - \alpha_2)} & \frac{\sqrt{2}J^2\Omega_1}{\alpha_2(2\Omega_1 - \alpha_2)} \\ \frac{\sqrt{2}J^2\Omega_1}{\alpha_2(2\Omega_1 - \alpha_2)} & \frac{2J^2(\Omega_1 - \alpha_2)}{\alpha_2(2\Omega_1 - \alpha_2)} \end{array} \right] \end{array}. \quad (\text{C2})$$

$$\hat{H}^D + \hat{V}_J + \hat{V}_I(t) = \begin{array}{l} |a,0\rangle \\ |b,0\rangle \\ |a,1\rangle \\ |b,1\rangle \\ |a,2\rangle \\ |b,2\rangle \end{array} \begin{array}{l} \begin{array}{cc} |a,0\rangle & |b,0\rangle \\ |a,1\rangle & |b,1\rangle \\ |a,2\rangle & |b,2\rangle \end{array} \left[\begin{array}{cccccc} -\frac{\Omega_1}{2} & 0 & \frac{\Omega_2 e^{i\delta t}}{2} - \frac{J}{2} & \frac{J}{2} & 0 & 0 \\ 0 & \frac{\Omega_1}{2} & -\frac{J}{2} & \frac{\Omega_2 e^{i\delta t}}{2} + \frac{J}{2} & 0 & 0 \\ \frac{\Omega_2 e^{-i\delta t}}{2} - \frac{J}{2} & -\frac{J}{2} & -\frac{\alpha_2}{2} - \frac{\Omega_1}{2} & 0 & \frac{\Omega_2 e^{i\delta t}}{\sqrt{2}} - \frac{J}{\sqrt{2}} & \frac{J}{\sqrt{2}} \\ \frac{J}{2} & \frac{\Omega_2 e^{-i\delta t}}{2} + \frac{J}{2} & 0 & -\frac{\alpha_2}{2} + \frac{\Omega_1}{2} & -\frac{J}{\sqrt{2}} & \frac{\Omega_2 e^{i\delta t}}{\sqrt{2}} + \frac{J}{\sqrt{2}} \\ 0 & 0 & \frac{\Omega_2 e^{-i\delta t}}{\sqrt{2}} - \frac{J}{\sqrt{2}} & -\frac{J}{\sqrt{2}} & -\frac{\Omega_1}{2} & 0 \\ 0 & 0 & \frac{J}{\sqrt{2}} & \frac{\Omega_2 e^{-i\delta t}}{\sqrt{2}} + \frac{J}{\sqrt{2}} & 0 & \frac{\Omega_1}{2} \end{array} \right] \end{array}. \quad (\text{C6})$$

Appendix D: Transition rates of the two-photon process

To quantify the visibility of the sideband transitions depending on the coupling strengths, we will employ the time-dependent perturbation theory that gives analytical expressions for the transition rates for single and multi-photon processes following [51].

Let us consider a time-dependent perturbation $\hat{V}(t) = \frac{\hbar\Omega_2}{2}(\hat{c}e^{i\omega_d t} + \hat{c}^\dagger e^{-i\omega_d t})$ to an unperturbed Hamiltonian \hat{H} . In the interaction picture, the Schrödinger equation reads

$$i\hbar\partial_t\psi(t) = \hat{V}_I(t)\psi(t),$$

where

$$\hat{V}_I(t) = e^{\frac{i}{\hbar}\hat{H}t}\hat{V}(t)e^{-\frac{i}{\hbar}\hat{H}t}.$$

The eigenstate of \hat{H} at energy E_j will be denoted as $|j\rangle$ whence

The normalized eigenvectors

$$|N\rangle = C_n|n\rangle + C_{n'}|n'\rangle, |N'\rangle = C'_n|n\rangle + C'_{n'}|n'\rangle \quad (\text{C3})$$

of the matrix are the desired zero-order superpositions. Next, we first-order correct them as usual:

$$|N\rangle + |N^1\rangle = \sum_{j=n,n'} C_j|j\rangle + \sum_{j\neq n,n'} |j\rangle \frac{\langle j|\hat{V}|N\rangle}{E_n - E_j}. \quad (\text{C4})$$

Similarly, the first-order correction for a non-degenerate state is

$$|m^1\rangle = \sum_{j\neq m} |m\rangle \frac{\langle j|\hat{V}|m\rangle}{E_m - E_j}. \quad (\text{C5})$$

it follows that

$$\langle j|\hat{V}_I(t)|i\rangle = e^{i\omega_{ij}t} \langle j|\hat{V}(t)|i\rangle,$$

where $\hbar\omega_{ij} = E_j - E_i$. Formally, we can write down the solution of the Schrödinger equation in the interaction picture corresponding to the initial state $|i\rangle$ as

$$|\psi_i(t)\rangle = |i\rangle - \frac{i}{\hbar} \int_{-\infty}^t d\tau_1 \hat{V}_I(\tau_1) |\psi_i(\tau_1)\rangle. \quad (\text{D1})$$

Solving Eq. D1 by simple iterations gives the series solution for it:

$$U(t, -\infty) = 1 + \sum_n U^{(n)}(t, -\infty), \quad (\text{D2})$$

$$U^{(n)}(t, -\infty) = \left(-\frac{i}{\hbar}\right)^n \int_{-\infty}^t d\tau_1 \hat{V}_I(\tau_1) \dots \int_{-\infty}^{\tau_{n-1}} d\tau_n \hat{V}_I(\tau_n), \quad (\text{D3})$$

where $U(t, -\infty)$ is the evolution operator. For a weak perturbation, this series may be truncated at a finite term n , and the n^{th} order transition amplitude $\langle f|U^{(n)}(t, -\infty)|i\rangle$ can be evaluated:

$$\begin{aligned} \langle f|U^{(1)}(t, -\infty)|i\rangle &= -\frac{i}{\hbar} \int_{-\infty}^t d\tau_1 \hat{V}_I(\tau_1) \\ &= -\frac{i\Omega_2}{2} \left[\int_{-\infty}^t d\tau_1 e^{i(\omega_f - \omega_d)\tau_1} \langle f|\hat{c}^\dagger|i\rangle + \int_{-\infty}^t d\tau_1 e^{i(\omega_f + \omega_d)\tau_1} \langle f|\hat{c}|i\rangle \right]. \end{aligned} \quad (\text{D4})$$

$$\begin{aligned} \langle f|U^{(2)}(t, -\infty)|i\rangle &= -\frac{1}{\hbar^2} \langle f| \int_{-\infty}^t d\tau_1 \hat{V}_I(\tau_1) \int_{-\infty}^{\tau_1} d\tau_2 \hat{V}_I(\tau_2) |i\rangle = \\ &= -\frac{1}{\hbar^2} \sum_j \int_{-\infty}^t d\tau_1 e^{i\omega_j \tau_1} \langle f|\hat{V}(\tau_1)|j\rangle \int_{-\infty}^{\tau_1} d\tau_2 e^{i\omega_j \tau_2} \langle j|\hat{V}(\tau_2)|i\rangle. \end{aligned} \quad (\text{D5})$$

Going over the long-time limit $t \rightarrow \infty$ in the final integral and collecting the terms belonging to the same delta functions gives [51]

$$\begin{aligned} \langle f|U^{(2)}(t, -\infty)|i\rangle &= \\ \frac{2\pi i \Omega_2^2}{4} &\left[\delta(\omega_f + 2\omega_d) \sum_j \frac{\langle f|\hat{c}|j\rangle \langle j|\hat{c}|i\rangle}{\omega_j + \omega_d} + \delta(\omega_f) \left(\sum_j \frac{\langle f|\hat{c}^\dagger|j\rangle \langle j|\hat{c}|i\rangle}{\omega_j + \omega_d} + \sum_j \frac{\langle f|\hat{c}|j\rangle \langle j|\hat{c}^\dagger|i\rangle}{\omega_j - \omega_d} \right) + \delta(\omega_f - 2\omega_d) \sum_j \frac{\langle f|\hat{c}^\dagger|j\rangle \langle j|\hat{c}^\dagger|i\rangle}{\omega_j - \omega_d} \right]. \end{aligned} \quad (\text{D6})$$

The probability of the two-photon transition from $|i\rangle$ to $|f\rangle$ is the square modulus of the corresponding amplitude, $P_{i \rightarrow f}^{(2)} = |\langle f|\hat{U}^{(2)}(\infty, -\infty)|i\rangle|^2$. The rate (probability per unit interaction time T) of absorption of 2 photons is defined as

$$W_{i \rightarrow f}^{(2)} = \lim_{T \rightarrow \infty} \frac{P_{i \rightarrow f}^{(2)}}{T}. \quad (\text{D7})$$

To cancel out one of the delta functions in the resulting expression, we can use the identity

$$\delta(\omega_f - \omega_i - 2\omega_d) = \frac{1}{2\pi} \lim_{T \rightarrow \infty} \int_{-T/2}^{T/2} e^{i(\omega_f - 2\omega_d)t} dt = \lim_{T \rightarrow \infty} \frac{T}{2\pi}.$$

For a two-photon emission:

$$\begin{aligned} W_{i \rightarrow f}^{(2)} &= \frac{\pi \Omega_2^4}{8} \left| \sum_j \frac{\langle f|\hat{c}|j\rangle \langle j|\hat{c}|i\rangle}{\omega_j + \omega_d} \right|^2 \delta(\omega_f + 2\omega_d) \\ &= R_{i \rightarrow f}^{(2)} \delta(\omega_f + 2\omega_d). \end{aligned} \quad (\text{D8})$$

For a two-photon absorption:

$$\begin{aligned} W_{f \rightarrow i}^{(2)} &= \frac{\pi \Omega_2^4}{8} \left| \sum_j \frac{\langle f|\hat{c}^\dagger|j\rangle \langle j|\hat{c}^\dagger|i\rangle}{\omega_j - \omega_d} \right|^2 \delta(\omega_f - 2\omega_d) \\ &= R_{f \rightarrow i}^{(2)} \delta(\omega_f - 2\omega_d). \end{aligned} \quad (\text{D9})$$

For our case, $\omega_d = \delta$ which leads to (14).

Appendix E: Measurement setup and methods

The sample was measured in a BlueFors LD250 dilution refrigerator at 16 mK. For the readout a Keysight PNA-L N5232A VNA was used. For the coherent excitation of the SAM, we used an Agilent MXG N5183B analog signal generator. The sample was flux biased using Yokogawa GS200 current sources (two for the flux lines and one for the external coil wrapped around the sample holder).

Input microwave lines were isolated from the high-temperature noise with 60 dB of attenuation (10 @ 4K, 10 @ 1K, 20 @ 100 and 16 mK) and custom IR filters. The effective on-chip attenuation between the drive line and the transmons was calculated in Sonnet to be around 70 dB @ 6 GHz. Coaxial flux-bias lines were attenuated by 20 dB @ 4K and IR filtered as well. Output path contained two 20 dB isolators and two amplifiers: a 4-14 GHz LNF amplifier at the 4 K stage and a room-temperature LNF amplifier.

As the main experimental method, we have employed the so-called two-tone spectroscopy which consists of exciting the SAM with monochromatic light at a certain frequency (first tone) until the steady state is reached while simultaneously measuring the signal transmission at the readout resonator frequency (second tone). This technique yields the average value of the joint measurement operator \hat{M} in the steady-state. To find the resonator frequency, we have been fitting its complex S_{21} response for each current with the second tone turned off with a method similar to the one described in our prior work [56] which employs the *circlefit* library [38]; the source code of our measurement script may be found at GitHub [60].

Appendix F: Sample fabrication

The device was fabricated on a high-resistivity Si wafer (10 kOhm-cm). First, the wafer was cleaned with Piranha, HF, and then coated with bilayer MMA/PMMA resist stack. The nominal after-bake thickness of the MAA and PMMA are 800 and 100 nm, respectively. The bilayer resist stack was exposed using a 50kV Raith Voyager EBL system and then developed. Next, the sample was placed into a high-vacuum electron-beam evaporation chamber (Plassys) and after a gentle ion-milling step, a double-angle evaporation technique at 10 degrees was used to deposit Al/AIOx/Al layer (25/45 nm). Finally, hot NMP followed by IPA was used to lift off the resist mask stack.

- [1] J. You and F. Nori, Atomic physics and quantum optics using superconducting circuits, *Nature* **474**, 589 (2011).
- [2] X. Gu, A. F. Kockum, A. Miranowicz, Y. xi Liu, and F. Nori, Microwave photonics with superconducting quantum circuits, *Physics Reports* **718-719**, 1 (2017).
- [3] A. Wallraff, D. I. Schuster, A. Blais, L. Frunzio, R.-S. Huang, J. Majer, S. Kumar, S. M. Girvin, and R. J. Schoelkopf, Strong coupling of a single photon to a superconducting qubit using circuit quantum electrodynamics, *Nature* **431**, 162 (2004).
- [4] I. Chiorescu, P. Bertet, K. Semba, Y. Nakamura, C. Harmans, and J. Mooij, Coherent dynamics of a flux qubit coupled to a harmonic oscillator, *Nature* **431**, 159 (2004).
- [5] P. Forn-Díaz, L. Lamata, E. Rico, J. Kono, and E. Solano, Ultrastrong coupling regimes of light-matter interaction, *Reviews of Modern Physics* **91**, 025005 (2019).
- [6] O. Astafiev, A. M. Zagoskin, A. Abdumalikov, Y. A. Pashkin, T. Yamamoto, K. Inomata, Y. Nakamura, and J. Tsai, Resonance fluorescence of a single artificial atom, *Science* **327**, 840 (2010).
- [7] C. Deng, J.-L. Orgiazzi, F. Shen, S. Ashhab, and A. Lupascu, Observation of floquet states in a strongly driven artificial atom, *Physical review letters* **115**, 133601 (2015).
- [8] C. Cohen-Tannoudji, J. Dupont-Roc, and G. Grynberg, Atom-photon interactions: basic processes and applications, *Atom-Photon Interactions: Basic Processes and Applications*, by Claude Cohen-Tannoudji, Jacques Dupont-Roc, Gilbert Grynberg, pp. 678. ISBN 0-471-29336-9. Wiley-VCH, March 1998, 678 (1998).
- [9] M. Baur, S. Filipp, R. Bianchetti, J. Fink, M. Göppl, L. Steffen, P. Leek, A. Blais, and A. Wallraff, Measurement of autler-townes and mollow transitions in a strongly driven superconducting qubit, *Physical review letters* **102**, 243602 (2009).
- [10] M. A. Sillanpää, J. Li, K. Cicak, F. Altomare, J. I. Park, R. W. Simmonds, G.-S. Paraoanu, and P. J. Hakonen, Autler-townes effect in a superconducting three-level system, *Physical review letters* **103**, 193601 (2009).
- [11] S. Novikov, J. Robinson, Z. Keane, B. Suri, F. Wellstood, and B. Palmer, Autler-townes splitting in a three-dimensional transmon superconducting qubit, *Physical Review B* **88**, 060503 (2013).
- [12] B. Suri, Z. Keane, R. Ruskov, L. S. Bishop, C. Tahan, S. Novikov, J. Robinson, F. Wellstood, and B. Palmer, Observation of autler-townes effect in a dispersively dressed jaynes-cummings system, *New Journal of Physics* **15**, 125007 (2013).
- [13] K. Koshino, H. Terai, K. Inomata, T. Yamamoto, W. Qiu, Z. Wang, and Y. Nakamura, Observation of the three-state dressed states in circuit quantum electrodynamics, *Physical review letters* **110**, 263601 (2013).
- [14] J. Braumüller, J. Cramer, S. Schlör, H. Rotzinger, L. Radtke, A. Lukashenko, P. Yang, S. T. Skacel, S. Probst, M. Marthaler, *et al.*, Multiphoton dressing of an anharmonic superconducting many-level quantum circuit, *Physical Review B* **91**, 054523 (2015).
- [15] Z. Peng, J. Ding, Y. Zhou, L. Ying, Z. Wang, L. Zhou, L. Kuang, Y.-x. Liu, O. Astafiev, and J. Tsai, Vacuum-induced autler-townes splitting in a superconducting artificial atom, *Physical Review A* **97**, 060503(R) (2018).
- [16] S. Gasparinetti, J.-C. Besse, M. Pechal, R. D. Buijs, C. Eichler, H. J. Carmichael, and A. Wallraff, Two-photon resonance fluorescence of a ladder-type atomic system, *Physical Review A* **100**, 033802 (2019).
- [17] C. Song, K. Xu, H. Li, Y.-R. Zhang, X. Zhang, W. Liu, Q. Guo, Z. Wang, W. Ren, J. Hao, H. Feng, H. Fan, D. Zheng, D.-W. Wang, H. Wang, and S.-Y. Zhu, Generation of multicomponent atomic schrödinger cat states of up to 20 qubits, *Science* **365**, 574 (2019).
- [18] Y. Ye, Z.-Y. Ge, Y. Wu, S. Wang, M. Gong, Y.-R. Zhang, Q. Zhu, R. Yang, S. Li, F. Liang, *et al.*, Propagation and localization of collective excitations on a 24-qubit superconducting processor, *Physical review letters* **123**, 050502 (2019).
- [19] F. Arute, K. Arya, R. Babbush, D. Bacon, J. C. Bardin, R. Barends, R. Biswas, S. Boixo, F. G. Brandao, D. A. Buell, *et al.*, Quantum supremacy using a programmable superconducting processor, *Nature* **574**, 505 (2019).
- [20] J. Fink, R. Bianchetti, M. Baur, M. Göppl, L. Steffen, S. Filipp, P. J. Leek, A. Blais, and A. Wallraff, Dressed collective qubit states and the tavis-cummings model in circuit qed, *Physical review letters* **103**, 083601 (2009).
- [21] P. Macha, G. Oelsner, J.-M. Reiner, M. Marthaler, S. André, G. Schön, U. Hübner, H.-G. Meyer, E. Il'ichev, and A. V. Ustinov, Implementation of a quantum metamaterial using superconducting qubits, *Nature communications* **5**, 5146 (2014).
- [22] K. V. Shulga, P. Yang, G. P. Fedorov, M. V. Fistul, M. Weides, and A. V. Ustinov, Observation of a collective mode of an array of transmon qubits, *JETP letters* **105**, 47 (2017).
- [23] P. Yang, J. D. Brehm, J. Leppäkangas, L. Guo, M. Marthaler, I. Boventer, A. Stehli, T. Wolz, A. V. Ustinov, and M. Weides, Probing the tavis-cummings level splitting with intermediate-scale superconducting circuits, *arXiv preprint arXiv:1810.00652* (2018).
- [24] A. Kou, W. Smith, U. Vool, R. Brierley, H. Meier, L. Frunzio, S. Girvin, L. Glazman, and M. Devoret, Fluxonium-based artificial molecule with a tunable magnetic moment, *Physical Review X* **7**, 031037 (2017).
- [25] J. Koch, M. Y. Terri, J. Gambetta, A. A. Houck, D. Schuster, J. Majer, A. Blais, M. H. Devoret, S. M. Girvin, and R. J. Schoelkopf, Charge-insensitive qubit design derived from the cooper pair box, *Physical Review A* **76**, 042319 (2007).
- [26] R. Barends, J. Kelly, A. Megrant, D. Sank, E. Jeffrey, Y. Chen, Y. Yin, B. Chiaro, J. Mutus, C. Neill, *et al.*, Coherent josephson qubit suitable for scalable quantum integrated circuits, *Physical review letters* **111**, 080502 (2013).
- [27] J. Majer, J. Chow, J. Gambetta, J. Koch, B. Johnson, J. Schreier, L. Frunzio, D. Schuster, A. A. Houck, A. Wallraff, *et al.*, Coupling superconducting qubits via a cavity bus, *Nature* **449**, 443 (2007).
- [28] J. Chow, L. DiCarlo, J. Gambetta, A. Nunnenkamp, L. S. Bishop, L. Frunzio, M. Devoret, S. Girvin, and R. Schoelkopf, Detecting highly entangled states with a joint qubit readout, *Physical Review A* **81**, 062325 (2010).
- [29] P. Tamarat, B. Lounis, J. Bernard, M. Orrit, S. Kummer, R. Kettner, S. Mais, and T. Basché, Pump-probe experiments with a single molecule: ac-stark effect and nonlinear optical response, *Physical review letters* **75**, 1514 (1995).
- [30] E. H. Ahmed, J. Huennekens, T. Kirova, J. Qi, and A. M. Lyyra, The autler-townes effect in molecules: observations, theory, and applications, in *Advances in Atomic, Molecular, and Optical Physics*, Vol. 61 (Elsevier, 2012) pp. 467–514.
- [31] S. Filipp, M. Göppl, J. Fink, M. Baur, R. Bianchetti, L. Steffen, and A. Wallraff, Multimode mediated qubit-qubit coupling and dark-state symmetries in circuit quantum electrodynamics, *Physical Review A* **83**, 063827 (2011).

- [32] L. DiCarlo, J. M. Chow, J. M. Gambetta, L. S. Bishop, B. R. Johnson, D. Schuster, J. Majer, A. Blais, L. Frunzio, S. Girvin, *et al.*, Demonstration of two-qubit algorithms with a superconducting quantum processor, *Nature* **460**, 240 (2009).
- [33] M. Kounalakis, C. Dickel, A. Bruno, N. K. Langford, and G. A. Steele, Tuneable hopping and nonlinear cross-kerr interactions in a high-coherence superconducting circuit, *npj Quantum Information* **4**, 1 (2018).
- [34] S. Poletto, J. M. Gambetta, S. T. Merkel, J. A. Smolin, J. M. Chow, A. Córcoles, G. A. Keefe, M. B. Rothwell, J. Rozen, D. Abraham, *et al.*, Entanglement of two superconducting qubits in a waveguide cavity via monochromatic two-photon excitation, *Physical review letters* **109**, 240505 (2012).
- [35] M. Hertzog, M. Wang, J. Mony, and K. Börjesson, Strong light-matter interactions: a new direction within chemistry, *Chemical Society Reviews* **48**, 937 (2019).
- [36] J. Hornibrook, J. Colless, I. C. Lamb, S. Pauka, H. Lu, A. Gosard, J. Watson, G. Gardner, S. Fallahi, M. Manfra, *et al.*, Cryogenic control architecture for large-scale quantum computing, *Physical Review Applied* **3**, 024010 (2015).
- [37] M. Hutchings, J. B. Hertzberg, Y. Liu, N. T. Bronn, G. A. Keefe, M. Brink, J. M. Chow, and B. Plourde, Tunable superconducting qubits with flux-independent coherence, *Physical Review Applied* **8**, 044003 (2017).
- [38] S. Probst, F. Song, P. Bushev, A. Ustinov, and M. Weides, Efficient and robust analysis of complex scattering data under noise in microwave resonators, *Review of Scientific Instruments* **86**, 024706 (2015).
- [39] M. Khalil, M. Stoutimore, F. Wellstood, and K. Osborn, An analysis method for asymmetric resonator transmission applied to superconducting devices, *Journal of Applied Physics* **111**, 054510 (2012).
- [40] I. Besedin and A. P. Menushenkov, Quality factor of a transmission line coupled coplanar waveguide resonator, *EPJ Quantum Technology* **5**, 1 (2018).
- [41] F. Yan, P. Krantz, Y. Sung, M. Kjaergaard, D. L. Campbell, T. P. Orlando, S. Gustavsson, and W. D. Oliver, Tunable coupling scheme for implementing high-fidelity two-qubit gates, *Physical Review Applied* **10**, 054062 (2018).
- [42] L. S. Bishop, Circuit quantum electrodynamics, arXiv preprint arXiv:1007.3520 (2010).
- [43] F. Beaudoin, J. M. Gambetta, and A. Blais, Dissipation and ultrastrong coupling in circuit qed, *Physical Review A* **84**, 043832 (2011).
- [44] G. Shavit, B. Horowitz, and M. Goldstein, Bridging between laboratory and rotating-frame master equations for open quantum systems, *Physical Review B* **100**, 195436 (2019).
- [45] S. Filipp, P. Maurer, P. Leek, M. Baur, R. Bianchetti, J. Fink, M. Göppl, L. Steffen, J. Gambetta, A. Blais, *et al.*, Two-qubit state tomography using a joint dispersive readout, *Physical review letters* **102**, 200402 (2009).
- [46] J. R. Johansson, P. D. Nation, and F. Nori, Qutip 2: A python framework for the dynamics of open quantum systems, *Computer Physics Communications* **184**, 1234 (2013).
- [47] https://github.com/vdrhtc/Examples/tree/master/transmon-simulations/two_transmons.
- [48] <http://qutip.org/docs/4.0.2/guide/guide-steady.html>.
- [49] T. Dittrich, P. Hänggi, G.-L. Ingold, B. Kramer, G. Schön, and W. Zwerger, *Quantum transport and dissipation*, Vol. 3 (Wiley-Vch Weinheim, 1998).
- [50] A. Rivas and S. F. Huelga, *Open quantum systems* (Springer, 2012).
- [51] F. H. Faisal, *Theory of multiphoton processes* (Springer Science & Business Media, 2013).
- [52] M. Malekakhlagh, A. Petrescu, and H. E. Türeci, Cutoff-free circuit quantum electrodynamics, *Physical review letters* **119**, 073601 (2017).
- [53] M. F. Gely, A. Parra-Rodriguez, D. Bothner, Y. M. Blanter, S. J. Bosman, E. Solano, and G. A. Steele, Convergence of the multi-mode quantum rabi model of circuit quantum electrodynamics, *Physical Review B* **95**, 245115 (2017).
- [54] D. M. Pozar, *Microwave engineering* (John Wiley & Sons, 2009).
- [55] J. Krupka, J. Breeze, A. Centeno, N. Alford, T. Claussen, and L. Jensen, Measurements of permittivity, dielectric loss tangent, and resistivity of float-zone silicon at microwave frequencies, *IEEE Transactions on microwave theory and techniques* **54**, 3995 (2006).
- [56] G. Fedorov and A. Ustinov, Automated analysis of single-tone spectroscopic data for cqed systems, *Quantum Science and Technology* **4**, 045009 (2019).
- [57] F. Solgun, D. P. DiVincenzo, and J. M. Gambetta, Simple impedance response formulas for the dispersive interaction rates in the effective hamiltonians of low anharmonicity superconducting qubits, *IEEE Transactions on Microwave Theory and Techniques* **67**, 928 (2019).
- [58] J. M. Chow, *Quantum information processing with superconducting qubits* (Yale University, 2010).
- [59] L. D. Landau and E. M. Lifshitz, *Quantum mechanics: non-relativistic theory*, Vol. 3 (Elsevier, 2013).
- [60] <https://github.com/vdrhtc/Measurement-automation/blob/master/lib2/FastTwoToneSpectroscopy.py>.